Supporting Information

Synthesis and growth mechanism of vertically aligned graphene sheets with precise control over the number of layers for Lithium-oxygen Battery

Atul Kumar[1,2], Akansha Dager*[3], Mukesh Kumar[4], Sudhanshu Shamra[4], Ankur Baliyan*[5,] Vinit Kumar*[6]

[1]Department of Electrical and Electronic Engineering, Amity University, Greater Noida 201308, India

[2] Amity Institute of Nanotechnology, Amity University Uttar Pradesh, Sector-125, Noida, UP-201313, India

[3]Graduate School of Nanobioscience, Yokohama City University, 22-2 Seto, Kanazawa-Ku, Yokohama 236-0027, Japan

[4]Department of Chemistry, Indian Institute of Technology Gandhinagar, Gandhinagar - 382055, Gujarat, India

[5]NISSAN ARC, LTD, 1-Natsushima-cho, Yokosuka, 236-0061, Japan

[6]Amity University Uttar Pradesh, Sector-125, Noida, UP-201313, India

Email: akanshadagar09@gmail.com, ankurbaliyan@gmail.com; vinitiitr@gmail.com; vkumar25@amity.edu

Contents

Figure. S17.

21. SEM images of nanostructures grown at NPs/SiO_2/Si substrate.
Figure. S18.

22. ML segmented image of carbon nanostructures at NPs/SiO_2/Si substrate.
Figure. S19.

23. HRTEM images of typical CNWs nanostructure grown at NPs/SiO_2/Si substrate.
Figure. S20.

24. Inward diffusion of carbon into SiO_2/Si substrate via SIMS.
Figure. S21.

25. SEM images of nanostructures grown at metallic (Cr/Cu/Ni) thin-film/Si substrate.
Figure. S22.

26. HRTEM images of typical CNWs nanostructure grown at metallic (Cr/Cu/Ni) thin-film/Si substrate.
Figure. S23.

27. SEM images of nanostructures at Cu thin-film/Si substrate.
Figure. S24.

28. Formation of a thick buffer layer.
Figure. S25.

29. Anisotropic growth of FLGs nanostructures.
Figure. S26.

30. Effect of higher methane gas flow rate on nucleation sites.
Figure. S27.

31. SEM images of 3D-HPG coated on CP and CC substrates via PECVD.
Figure. S28.

32. HRTEM images of typical 3D-HPG nanostructure grown at CC substrate.
Figure. S29.

33. The pore size distribution of 3D-HPG nanostructure.
Figure. S30.

34. Table T3: Surface area and total pore volume 3D-HPGs nanostructures.

35. XPS wide and a detailed scan of C 1s of 3D-HPG nanostructures on CP substrate.
Figure. S31.

36. XPS wide and a detailed scan of C 1s of 3D-HPGs nanostructures on CC substrate.
Figure. S32.

37. Estimation of Electrochemical Surface Area (ECSA) for CP, 3D-HPG coated CP, CC, and 3D-HPG coated CC.
Figure. S33.

38. Charge and Discharge profile of 3D-HPG coated CP and CC electrodes at 0.1 mA and 0.3 mA.
Figure. S34.

39. SEM image of the charge and discharge 3D-HPG coated CP.
Figure. S35.

1. Schematic diagram of a typical Li-O_2 battery.

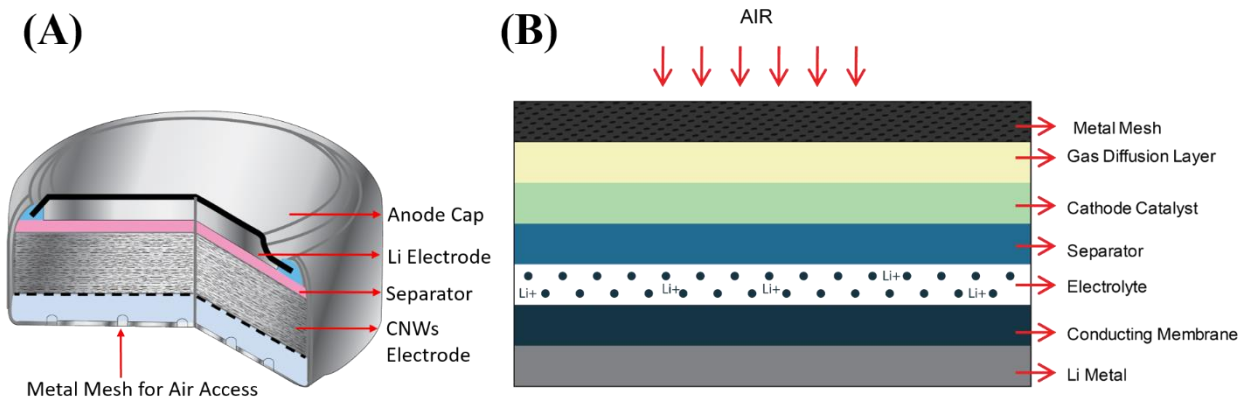

Figure S1: Illustrates the schematics of a typical Li-O_2 battery. (A) LIB schematics. (B) Cross-sectional view of layered Li-Air Battery. A typical Li-Air Battery comprises; negative electrode of Li metal, a positive porous electrode, separator, and non-aqueous Li electrolyte. During discharge, oxygen (O_2) is reduced and combined with Li^+ at the positive electrode, forming a discharge product that fills the positive porous electrode. During the charging process, the previously formed product at the positive porous electrode should be thoroughly removed.

2. Characterization of optical emission spectroscopy (OES).

The plasma was characterized by optical emission spectroscopy (OES). The spectrometer (HR-4000, Ocean optics) combined with an optical fiber (core diameter: 600 mm) was utilized to record the plasma spectra. The tip of the optical fiber was attached to the substrate holder in order to observe the plasma from the below. The position of the substrate holder was set (D = 50 mm), so that the entire plasma can be investigated.

3. Table T1: CNWs nanostructures synthesized with various process parameters.

Sample Name	**Methane** (SCCM)	**Hydrogen** (SCCM)	**Temperature (°C)**	**Distance (mm)**	**Pressure (Torr)**	Nanostructures (CNW/FLG)
C_2H_{30}	2	30	800	20	0.20	--
C_3H_{30}	3	30	800	20	0.20	CNW
C_4H_{30}	4	30	800	20	0.20	FLG
C_5H_{30}	5	30	800	20	0.20	FLG
C_7H_{30}	7	30	800	20	0.20	FLG
$C_{10}H_{25}$	10	25	800	20	0.20	CNW
$C_{15}H_{20}$	15	20	800	20	0.20	CNW
$C_{20}H_{15}$	20	15	800	20	0.20	CNW
$C_{25}H_{10}$	25	10	800	20	0.20	CNW
$C_{30}H_5$	30	5	800	20	0.20	CNW
C_5H_{30}	5	30	500	20	0.20	CNW
C_5H_{30}	5	30	600	20	0.20	CNW
C_5H_{30}	5	30	700	20	0.20	CNW
C_5H_{30}	5	30	800	30	0.20	CNW
C_5H_{30}	5	30	800	40	0.20	CNW
C_5H_{30}	5	30	800	50	0.20	CNW
C_5H_{30}	5	30	800	20	0.40	CNW
C_5H_{30}	5	30	800	20	0.80	CNW
C_5H_{30}	5	30	800	20	1.20	CNW

4. SEM image of CNWs nanostructure synthesized with respect to process parameters.

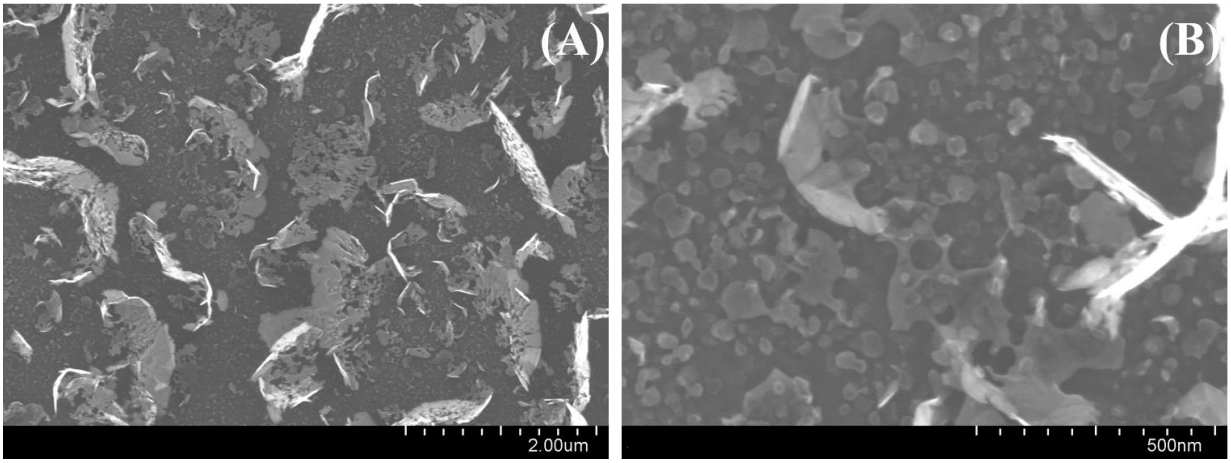

Figure S2: Carbon nanostructure grown with different process parameters. (A) Carbon nanostructures grown at 800 °C, distance between the quartz disk and the substrate (D = 20) at CH_4 and H_2 gas flow of 30 and 5 sccm, respectively. (B) Carbon nanostructures grown at 800 °C, distance between the quartz disk and the substrate (D = 40) at CH_4 and H_2 gas flow of 5 and 30 sccm, respectively.

5. HRTEM images of graphene sheets in FLG nanostructures.

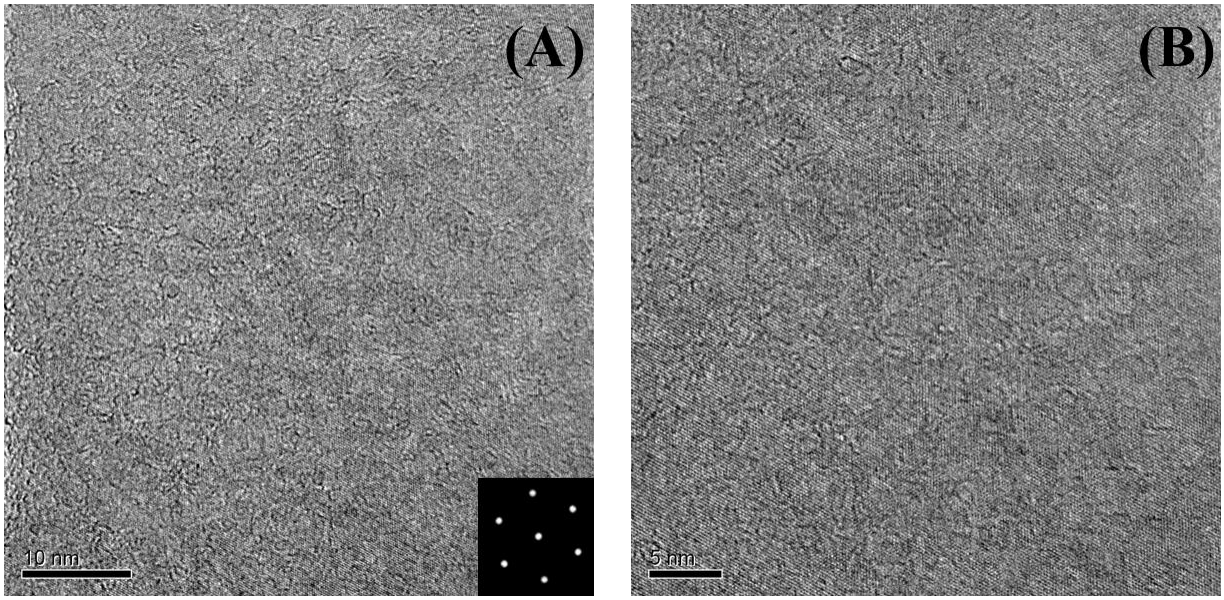

Figure S3: FLG nanostructure grown with lower CH_4 and H_2 gas flow rate of 5 and 30 sccm, respectively. (A) Low resolution HRTEM image shows the long range graphene sheet. Inset shows FFT of the FLG, it has hexagon signature, indicating the evidence of perfect graphene sheet. (B) Low resolution HRTEM image of FLG shows atomic structure of graphene layer, individual atoms can be seen.

6. Optical emission spectra (OES) of the excited CH_4 and H_2 plasma.

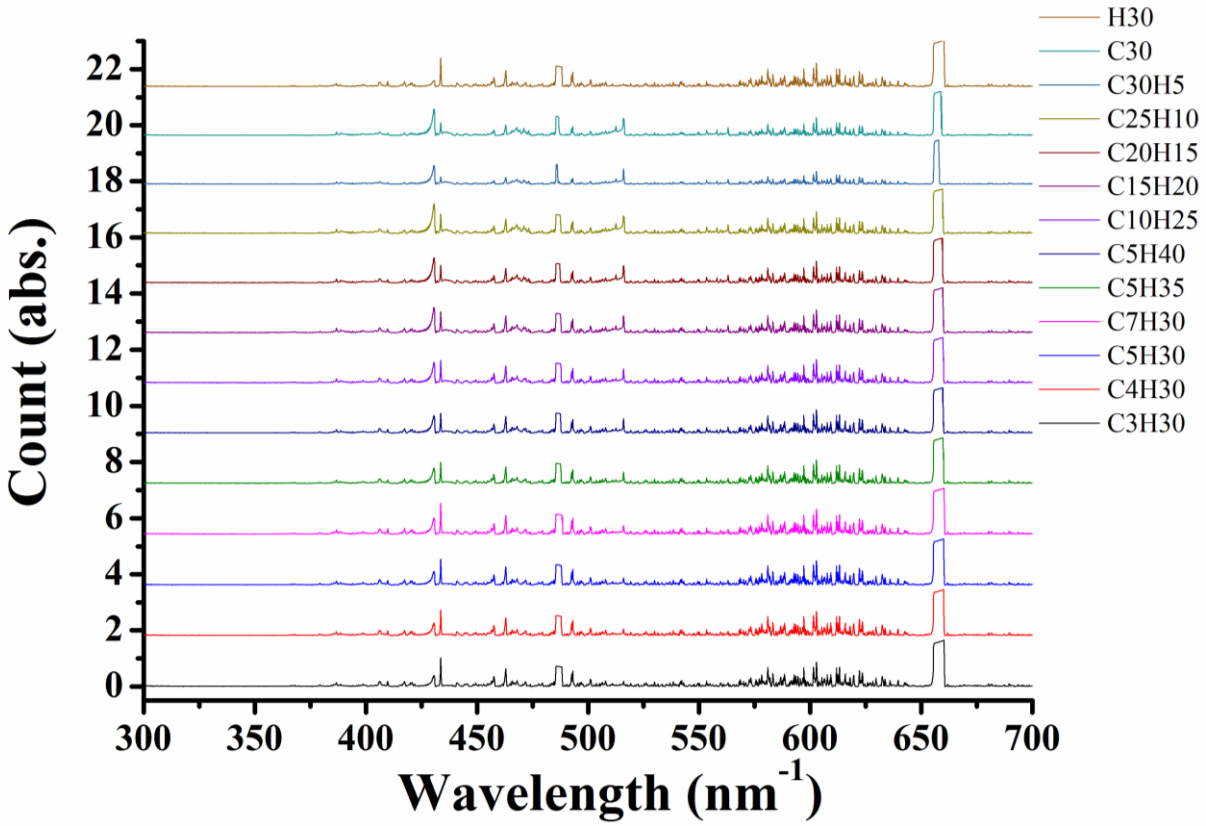

Figure S4: Optical emission spectrums (OES) of the excited CH_4 and H_2 plasma. The OES results depict peaks at 658.1, 486.8, 434.6, 463.7, and 516.3 nm, and they were ambiguously assigned to H_α, H_β, H_γ, secondary-hydrogen and C_2 molecules, respectively. The lower intensity of the Fulcher band in the 575-635 nm region denotes that the plasma has a high degree of CH_4 and H_2 dissociation. It is apparent that as methane concentration increases, the emission intensity of C_2 molecules also increased gradually.

7. **Variance of optical emission spectrums (OES) of the excited CH_4 and H_2 plasma.**

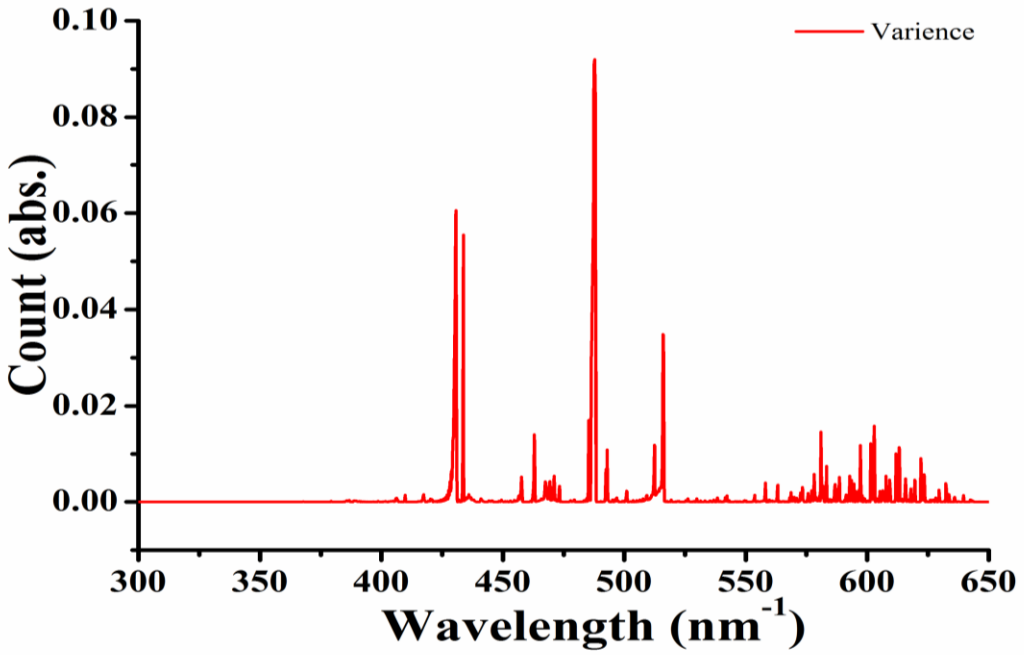

Figure S5: variance of optical emission spectrums (OES) of the excited CH_4 and H_2 plasma, OES data was truncated beyond 650 nm^{-1} for better visualization.

8. **PCA analysis results of OES data-set.**

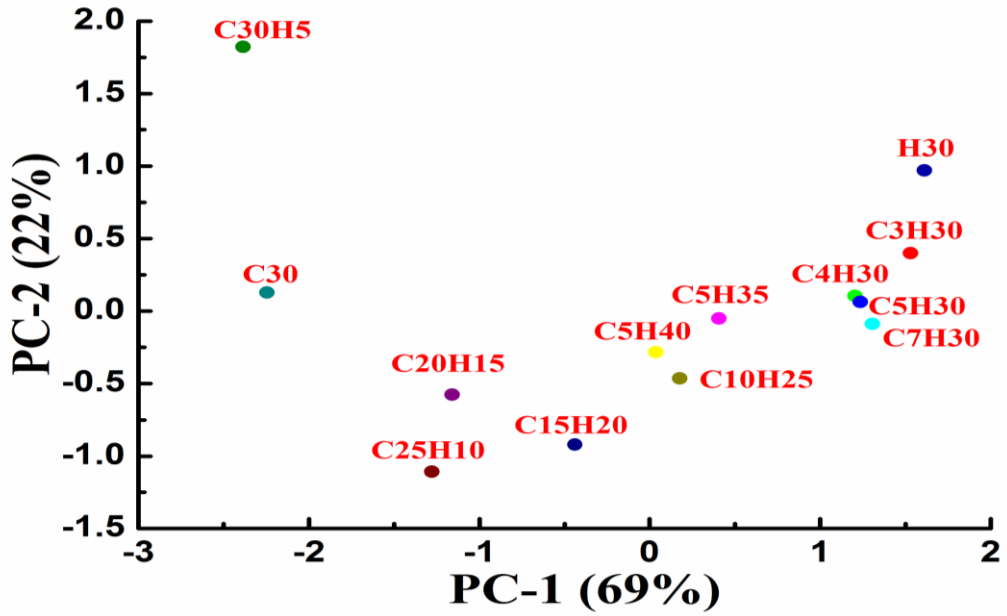

Figure S6: First two principal components (PCs) explain more than 91.0 % of the OES data-set. The lower amount of CH_4 gas flow rate (4, 5, and 7 sccm), which promotes the formation of FLGs, is negatively correlated to the high amount of CH_4 gas flow rate.

9. MCR analysis results of OES data-set.

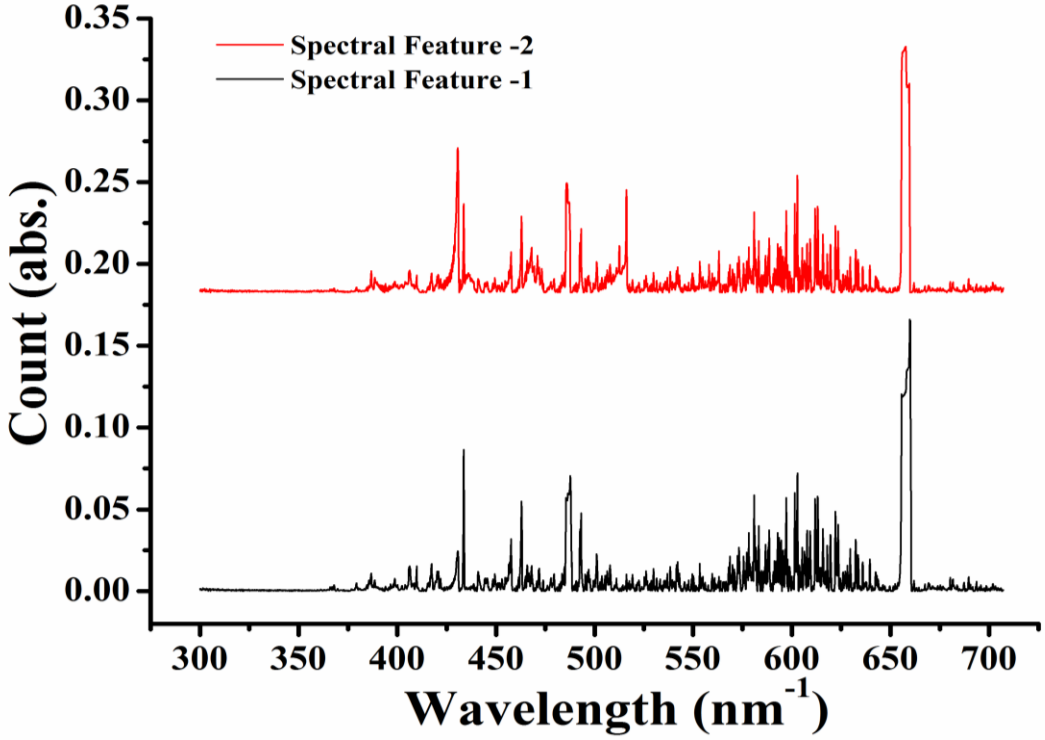

Figure S7: MCR analysis of OES had two essential features; (i) 'spectral feature-1' and, (ii) The 'spectral feature-2'. The 'spectral feature-1' has a close resemblance with lower methane OES spectra compared to the 'spectral feature-2' and vice versa.

10. The concentration of 'spectral feature-1' & 'spectral feature-2' in excited CH_4 and H_2 plasma.

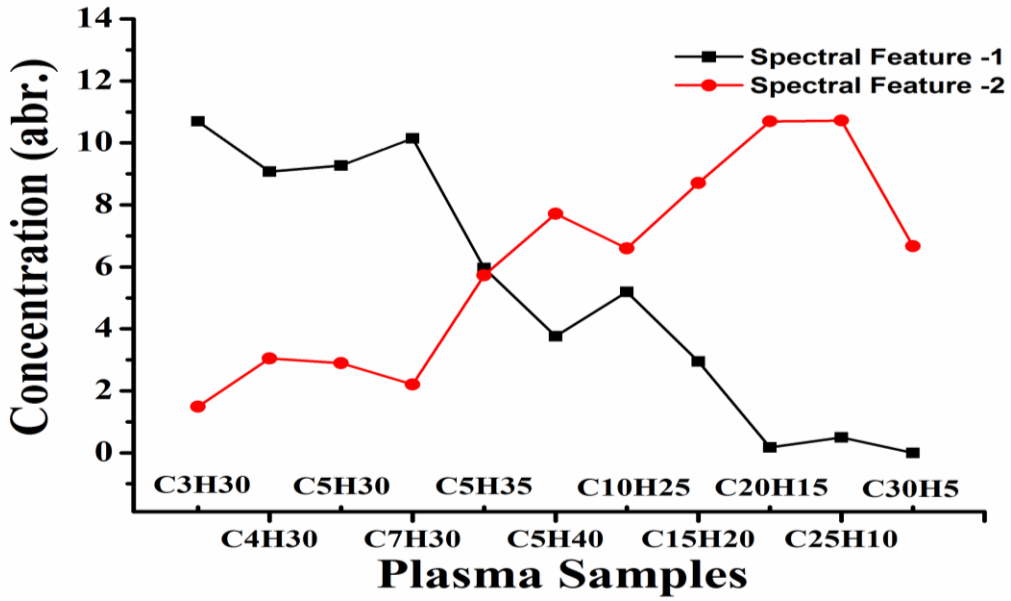

Figure S8: MCR analysis concentration contribution. It is obvious from the results that the 'spectral feature-1' concentration is higher compared to the 'spectral feature-2' at a lower methane gas flow rate and vice versa.

11. XPS (wide and detailed scan) of FLGs nanostructures.

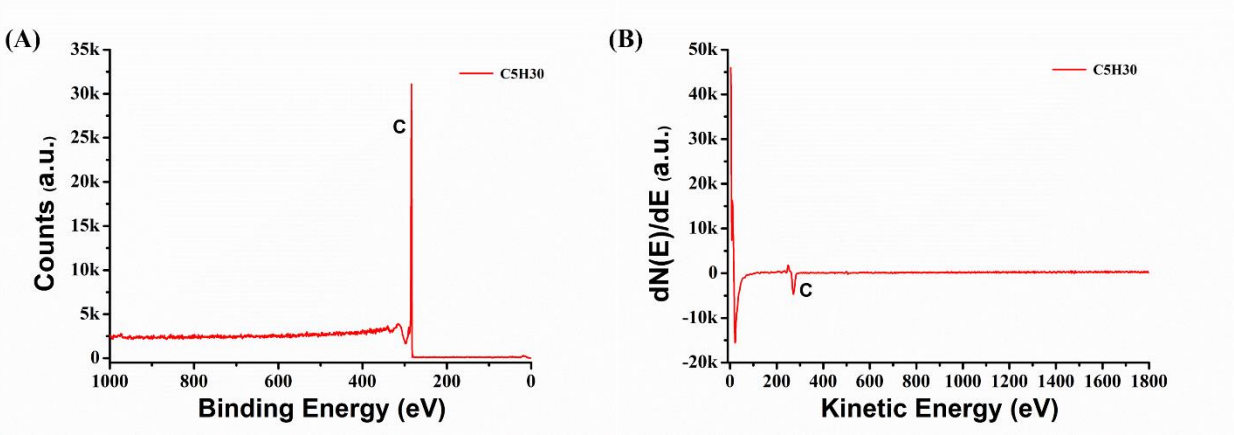

Figure S9: XPS and Auger of FLGs nanostructures grown at CH_4 and H_2 gas flow rate of 5 and 30 sccm, respectively. (A) XPS of FLGs nanostructures exhibit no other peak than carbon; no trace amount of oxygen was found in the wide scan. (B) Auger line shape C (KVV) transition provides qualitative insight into the structural arrangement of the carbon atoms in FLGs. The Transition peak at ~270.0 eV was detected and assigned to C (KVV) transition, its shape has a close resemblance to the single-crystal graphite/FLGs.

12. 3D-AFM and line scan plot of FLGs deposited on a silicon substrate.

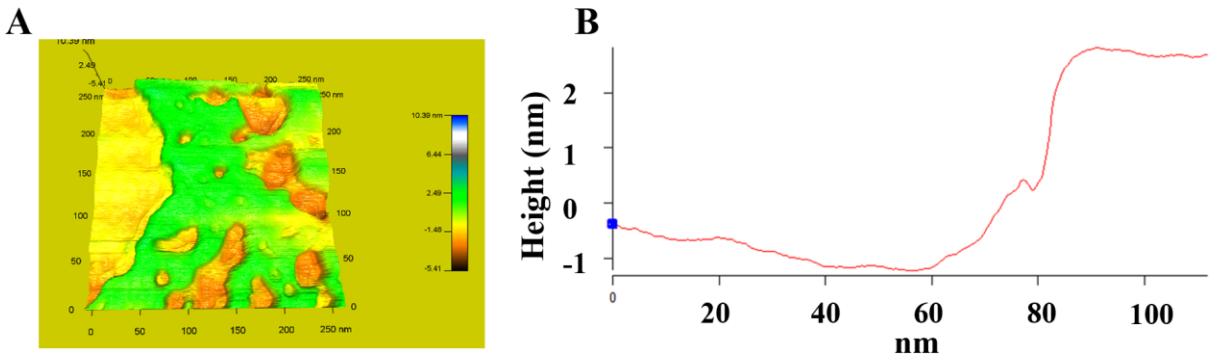

Figure S10: FLGs deposited on a silicon substrate. (A) FLGs nanostructures have multiple pores. Such pores were already observed in the SEM images. (B) The line scan in shows that FLGs have a thickness of ~3.0 nm, i.e., FLGs was composed of around four graphene layers.

13. Raman spectra of all the specimens with respect to the change in CH_4 and H_2 gas flow rate.

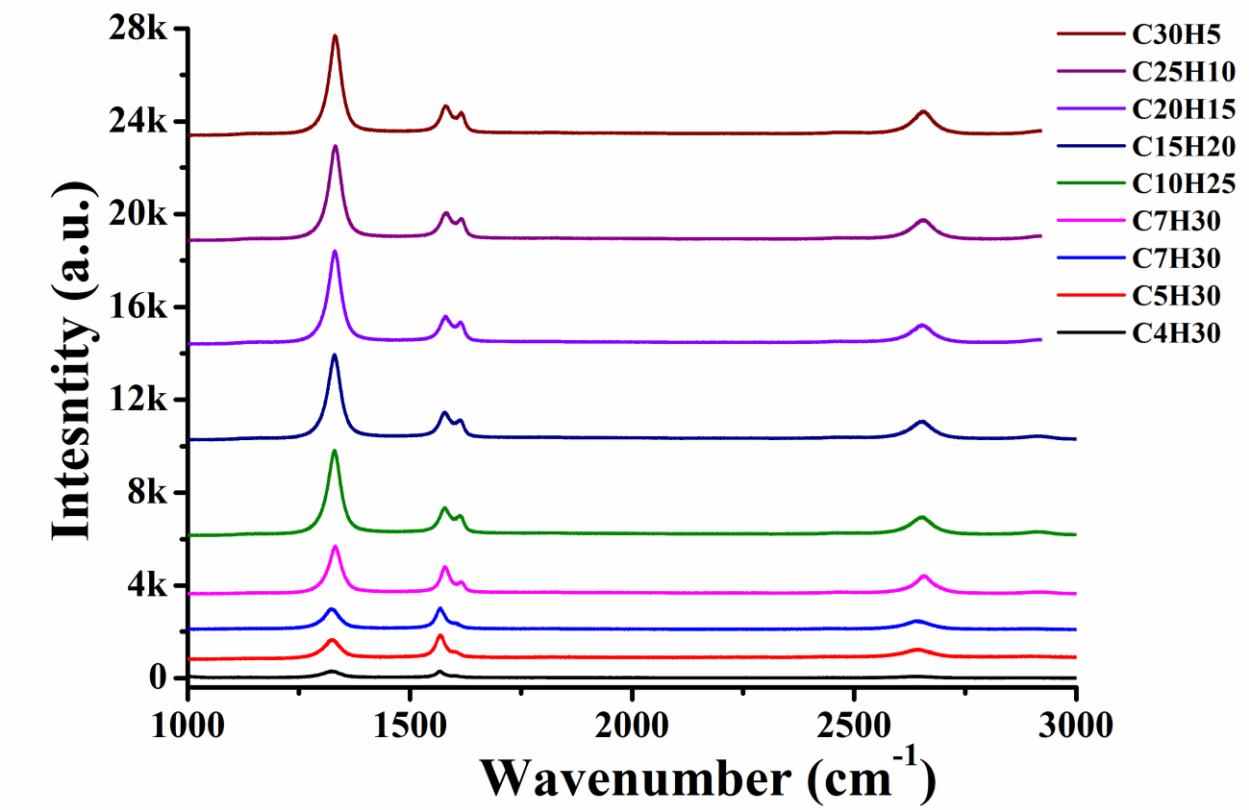

Figure S11: Raman spectra of carbon nanostructures. As the CH_4 gas flow rate to increases, the intensity ratio of the G band to the D band continues to get lower, and it corresponds to the amount of increase in defects and edge effects. The lower amount of CH_4 gas flow rate promotes the formation of FLGs, whereas the higher methane gas flow rate promotes the CNWs nanostructure formation.

14. Table T2: Raman peak position and intensity ratio for all the nanostructure grown on silicon substrate.

Sample Name	Position D band (cm^{-1})	Position G band (cm^{-1})	Position 2D band (cm^{-1})	I_D/I_G	I_G/I_{2D}	Nanostructures (CNW/FLG)
C_2H_{30}	1326	1581	2661	0.37	1.37	--
C_3H_{30}	1327	1576	2660	0.56	3.20	CNW
C_4H_{30}	1325	1577	2655	1.04	2.40	FLG
C_5H_{30}	1326	1578	2654	1.75	2.80	FLG
C_7H_{30}	1325	1577	2655	0.82	2.73	FLG
$C_{10}H_{25}$	1331	1580	2661	0.56	1.44	CNW
$C_{15}H_{20}$	1329	1580	2660	0.32	1.46	CNW
$C_{20}H_{15}$	1330	1579	2661	0.31	1.53	CNW
$C_{25}H_{10}$	1330	1580	2663	0.29	1.32	CNW
$C_{30}H_5$	1330	1580	2661	0.32	1.24	CNW

15. Inward diffusion of carbon into silicon substrate via SIMS.

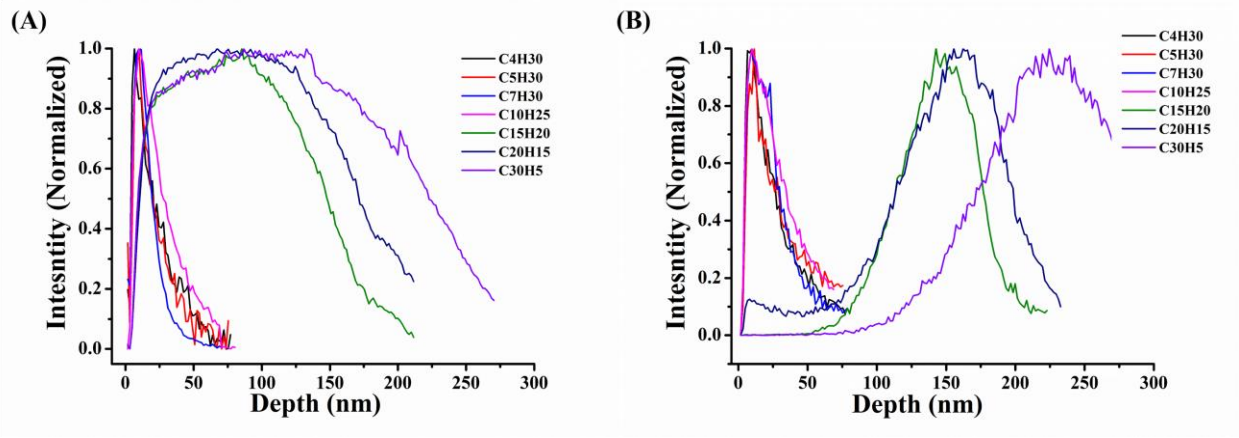

Figure S12: SIMS investigation of carbon nanostructure at grown at silicon substrate. (A) Carbon diffusion, with an increase in the CH_4 gas flow rate, the carbon diffuses deeper into the silicon' subsurface and promotes bulk diffusion and vice versa. (B) An intermetallic layer of SiC formation was observed. The SiC penetration depth profile suggests that carbon diffusion has two separate regimes, namely limited-diffusion (< ~25 nm) and bulk-diffusion (> ~25 nm).

16. SEM images of nanostructures grown at SiO_2/Si substrate.

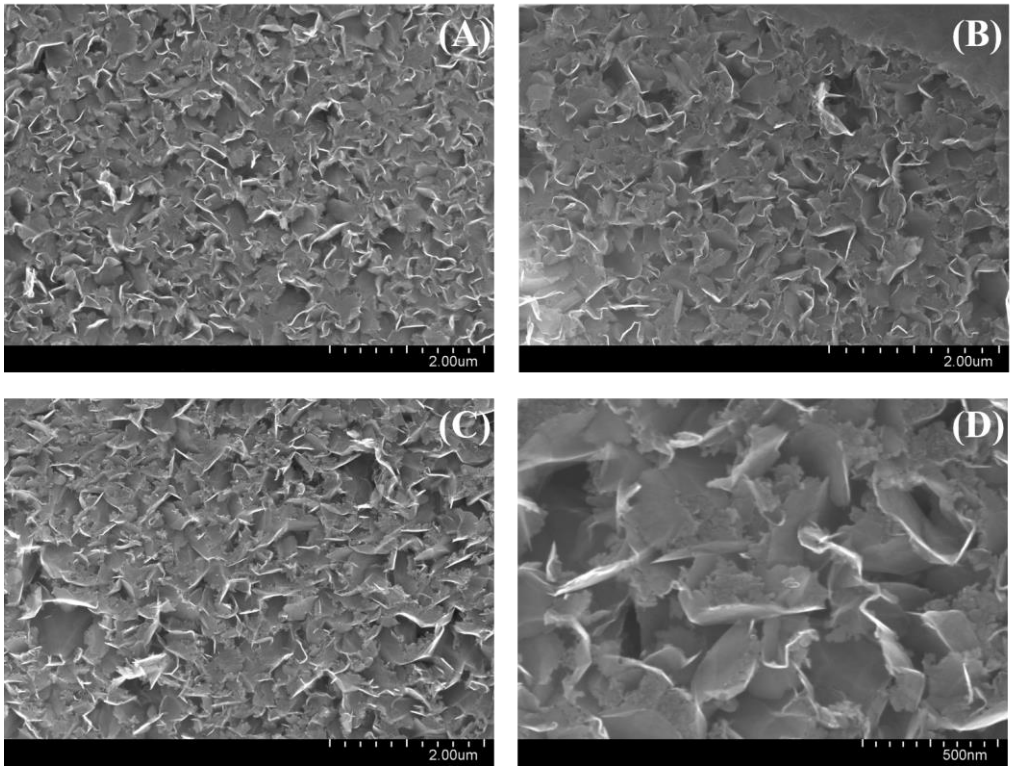

Figure S13: SEM images of nanostructures grown at SiO_2/Si substrate. (A) 100 nm SiO_2/Si substrate. (B) 200 nm SiO_2/Si substrate. (C) 300 nm SiO_2/Si substrate. (D) High resolution image of 200 nm SiO_2/Si substrate. The amount of amorphous carbon formation increases with an increase in the SiO_2 thickness on silicon substrate.

17. ML segmented image of carbon nanostructures at SiO_2/Si substrate.

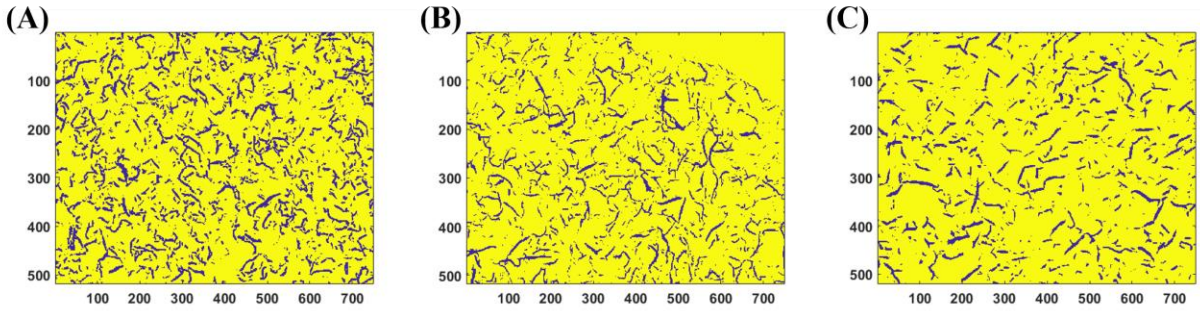

Figure S14: ML segmented images of carbon nanostructures grown at SiO_2/Si substrate, ML based Illastic tool was used for pixel classification. (A) 100 nm SiO_2/Si substrate. (B) 200 nm SiO_2/Si substrate. (C) 300 nm SiO_2/Si substrate. ML image segmentation reveals that the thinner SiO_2/Si specimen has higher nucleation sites and a lower amount of amorphous carbon nanostructure compared with thick SiO_2/Si specimen and vice versa.

18. HRTEM images of typical CNWs nanostructure.

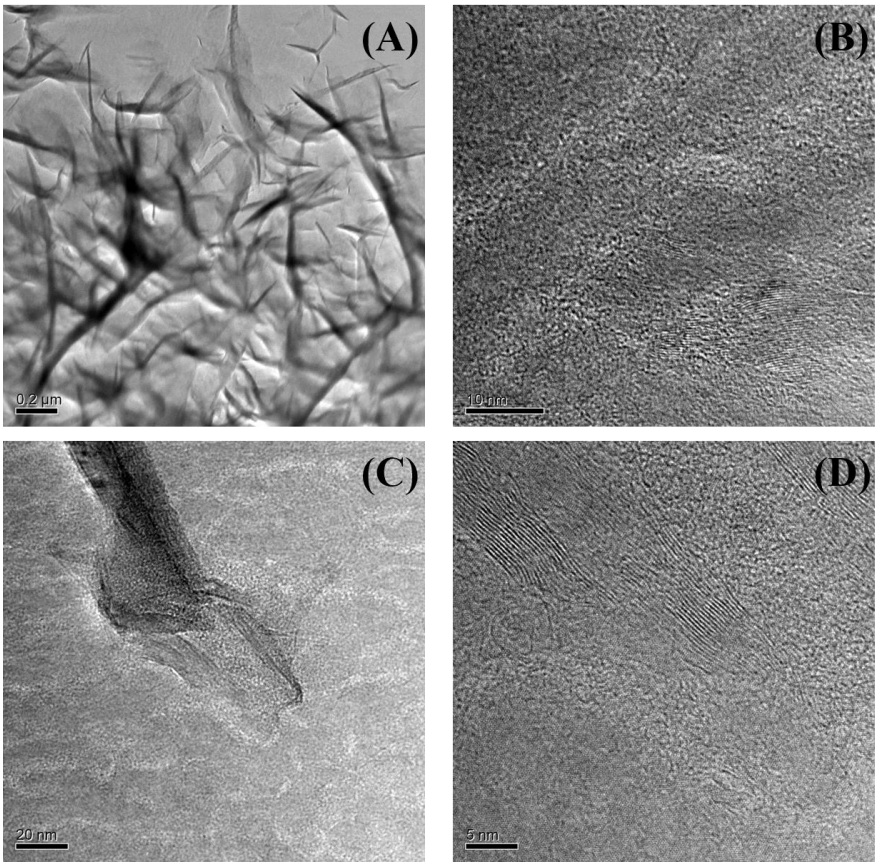

Figure S15: Carbon nanostructure grown with CH_4 and H_2 gas flow rate of 30 and 5 sccm, respectively. (A) & (C). Low resolution image shows branched nanostructure of CNWs. (B) & (D) High-resolution images shows as-grown CNWs have many secondary fins and such irregularities give rise to the thick CNWs formation.

19. Inward diffusion of carbon into SiO_2/Si substrate via SIMS.

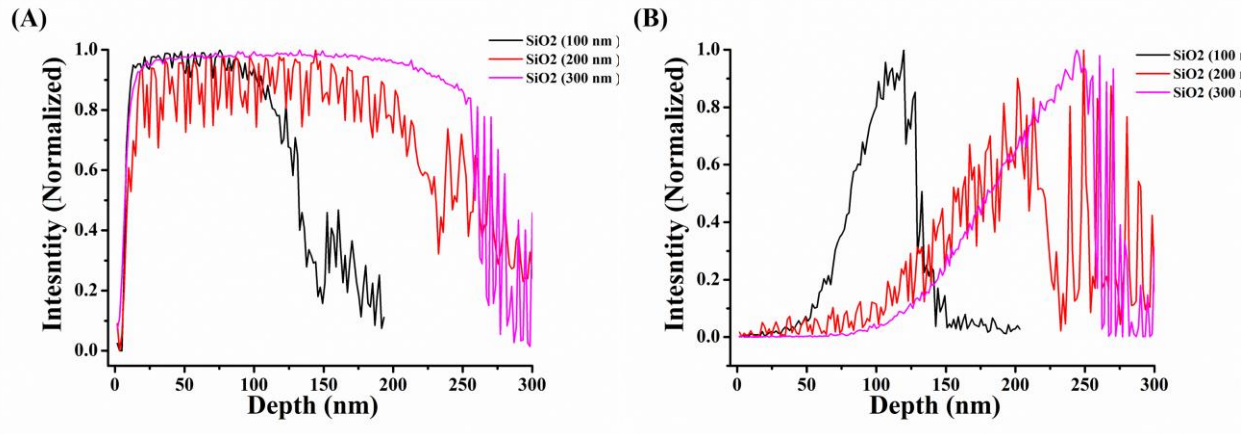

Figure S16: SIMS investigation of carbon nanostructure at grown at SiO_2/Si substrate. (A) Carbon diffuse deeper into the SiO_2/Si substrate. (B) Unlike the silicon substrate, a thick SiC buffer layer was formed, the SiC penetration depth profile of the SiO_2/Si substrate signifies that carbon diffuses via bulk-diffusion (> ~100 nm).

20. Monolayer of nanoparticles deposited on the SiO_2/Si substrate.

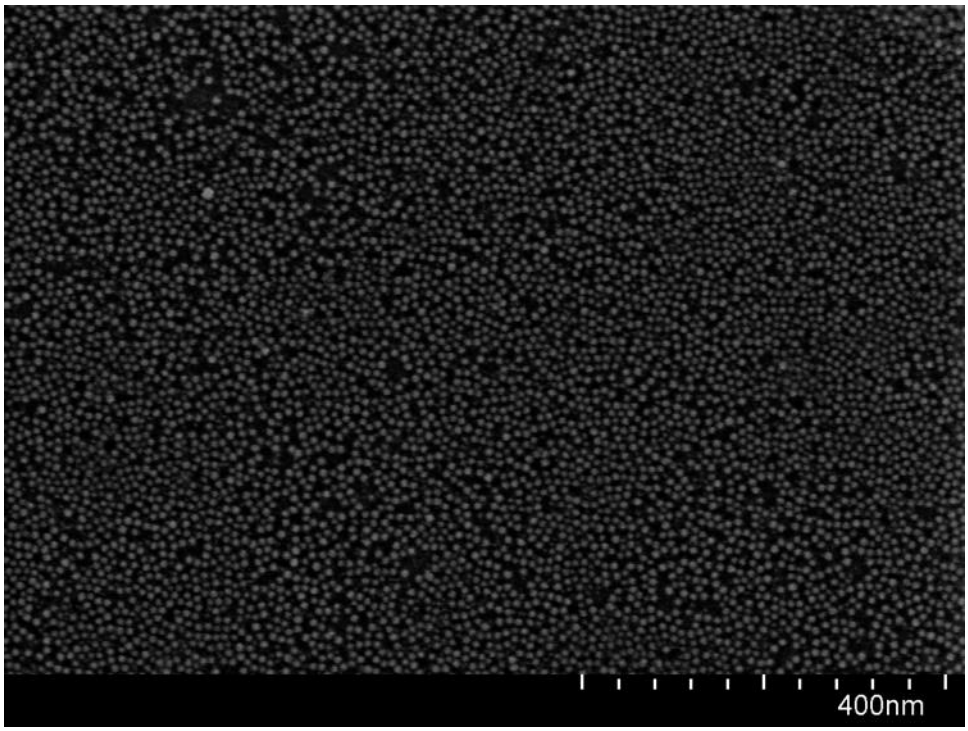

Figure S17: A monolayer of NPs/100 nm-SiO_2/Si was coated using the spin coating technique. SEM images depicts the monolayer of nanoparticles onto the silicon oxide substrate. The average size of NPs was 7.53 ± 0.11 nm.

21. SEM images of nanostructures grown at NPs/SiO_2/Si substrate.

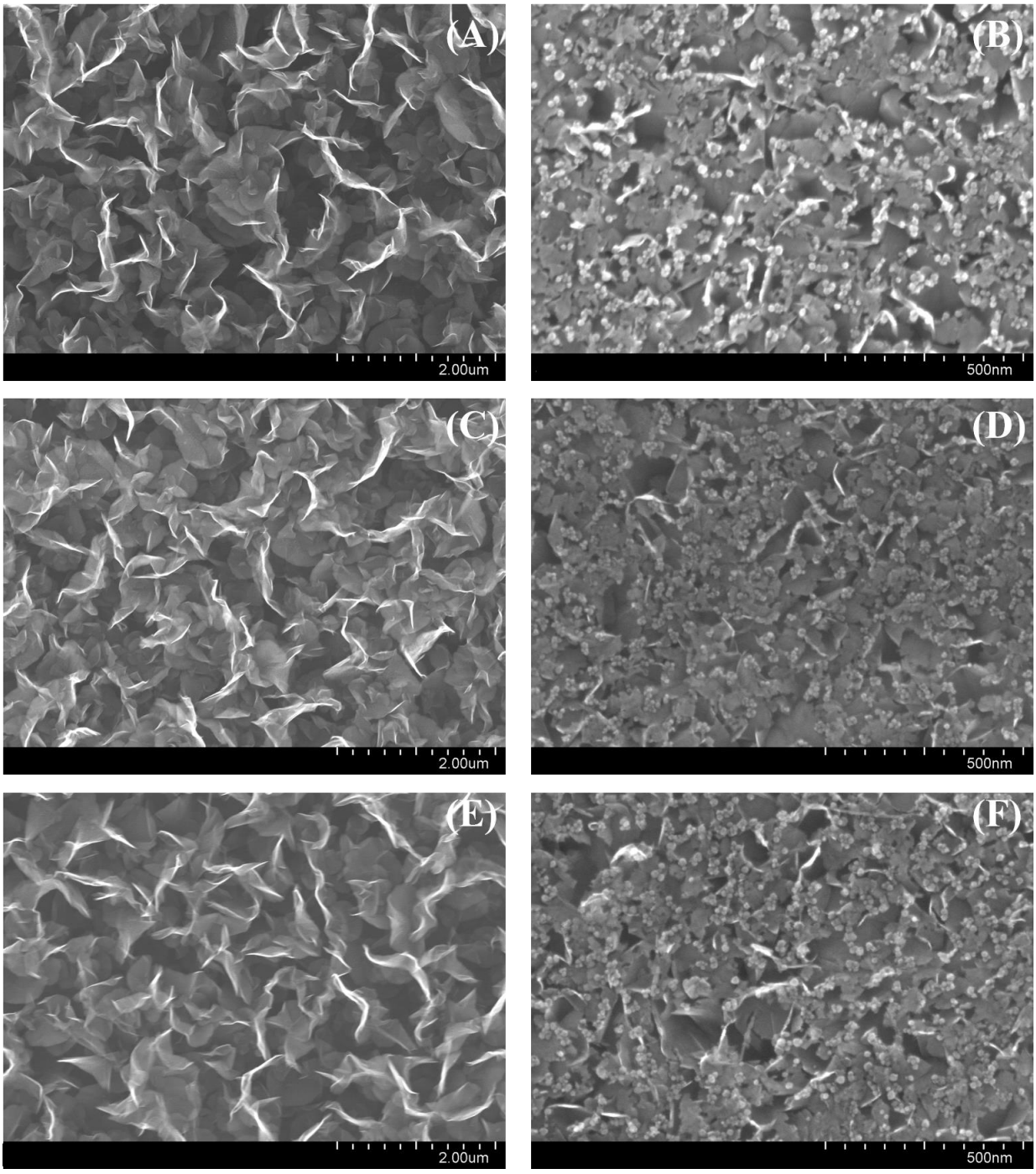

Figure S18: SEM images of nanostructures grown at NP/SiO_2/Si substrate, irrespective of the NP and SiO2 thickness the CNWs were formed and no FLGs nanostructure was formed. (A) NP/100 nm SiO_2/Si substrate. (B) NP/200 nm SiO_2/Si substrate. (C) NP/300 nm SiO_2/Si substrate. The amount of amorphous carbon and nucleation sites were roughly the same irrespective of the substrate.

22. ML segmented image of carbon nanostructures at NPs/SiO_2/Si substrate.

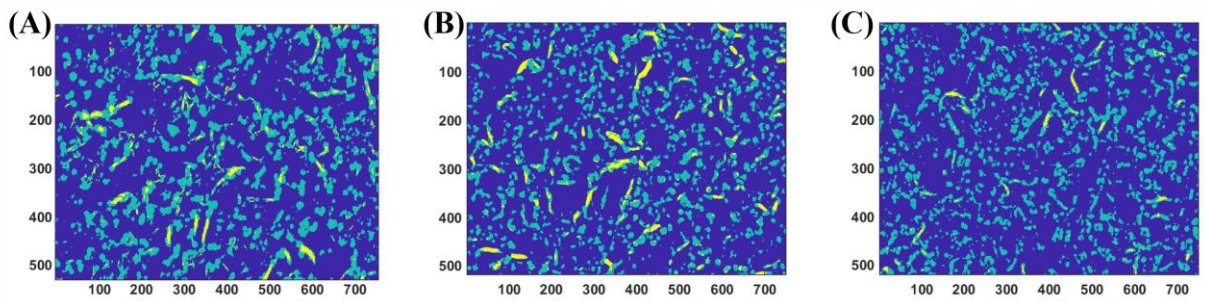

Figure S19: ML segmented images of carbon nanostructures grown at NP/SiO_2/Si substrate, ML based Illastic tool was used for pixel classification; blue (amorphous carbon), sky-blue (NPs) and yellow color (CNWs sites) . (A) NPs/100 nm SiO_2/Si substrate. (B) NPs/200 nm SiO_2/Si substrate. (C) NPs/300 nm SiO_2/Si substrate. ML image segmentation reveals the amount of amorphous carbon and nucleation sites were roughly the same irrespective of the substrate.

23. HRTEM images of typical CNWs nanostructure grown at NPs/SiO_2/Si substrate.

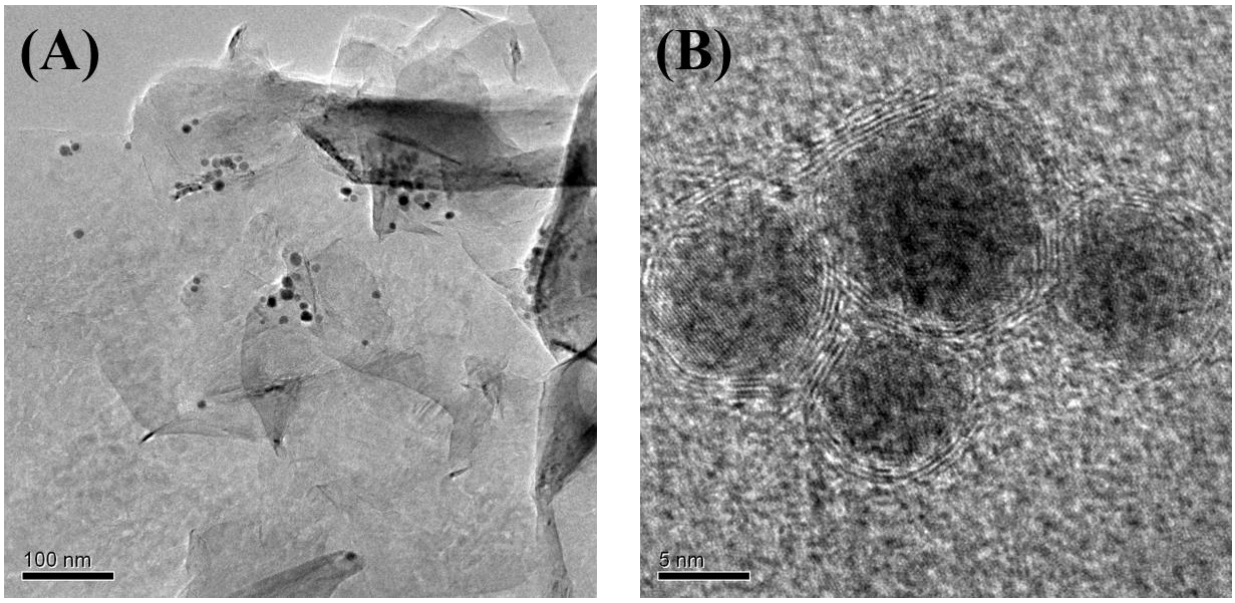

Figure S20: The HRTEM images of CNWs nanostructures. (A) High resolution images show that NPs act as the nucleation sites for the CNWs nanostructure. (B) Some of the NPs were inactivated and were found lying on the CNWs.

24. Inward diffusion of carbon into SiO_2/Si substrate via SIMS.

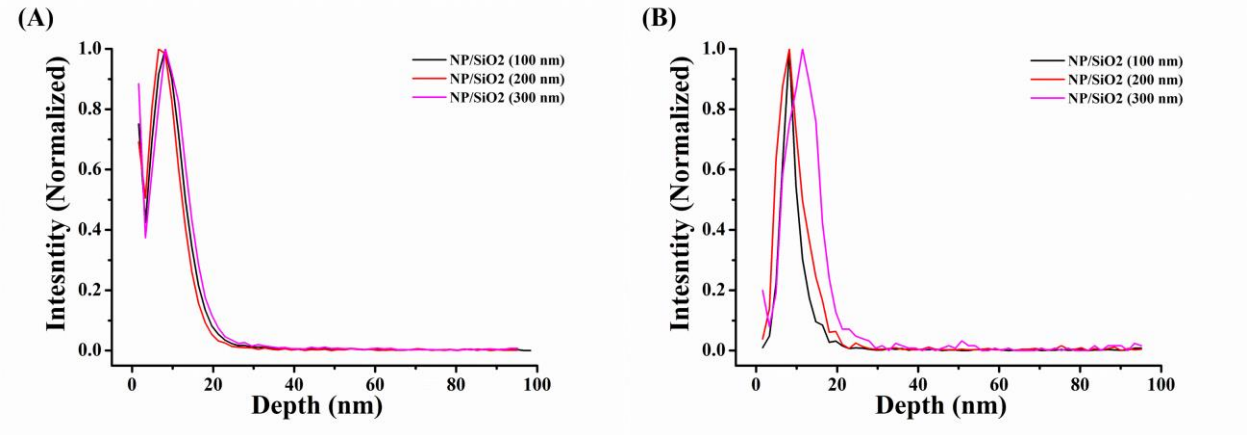

Figure S21: SIMS investigation of carbon nanostructure at grown at NPs/SiO_2/Si substrate. (A) NPs discourage carbon diffusion into the silicon-oxide subsurface. (B) The formation of the SiC layer was minimal on to the NPs' coated silicon-oxide substrates. NPs shield the silicon-oxide layer and discourage carbon diffusion into the silicon-oxide subsurface.

25. SEM images of nanostructures grown at metallic (Cr/Cu/Ni) thin-film/Si substrate.

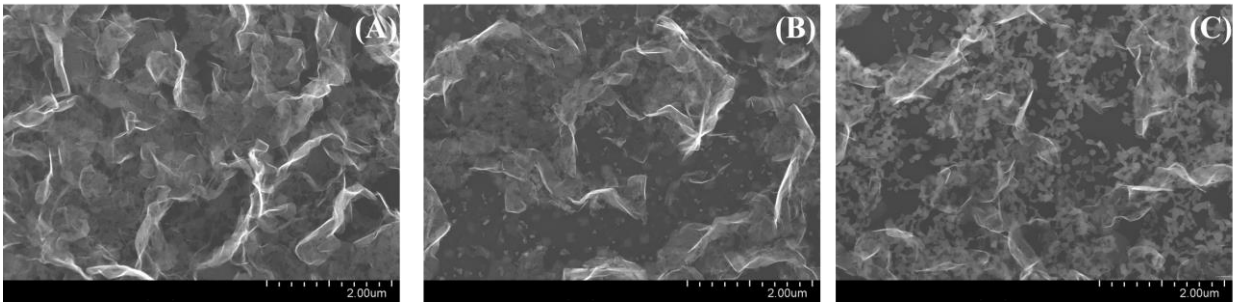

Figure S22: SEM image of carbon nanostructures grown on metal-coated silicon substrates. (A) Chromium, (B) Copper, (C) Nickel. Plasma exposure breakdown the metal film into small size NPs. The amount of CNWs nanostructure formed on a metal-coated substrate was less than the iron NPs coated on a silicon oxide substrate.

26. HRTEM images of typical CNWs nanostructure grown at metallic (Cr/Cu/Ni) thin-film/Si substrate.

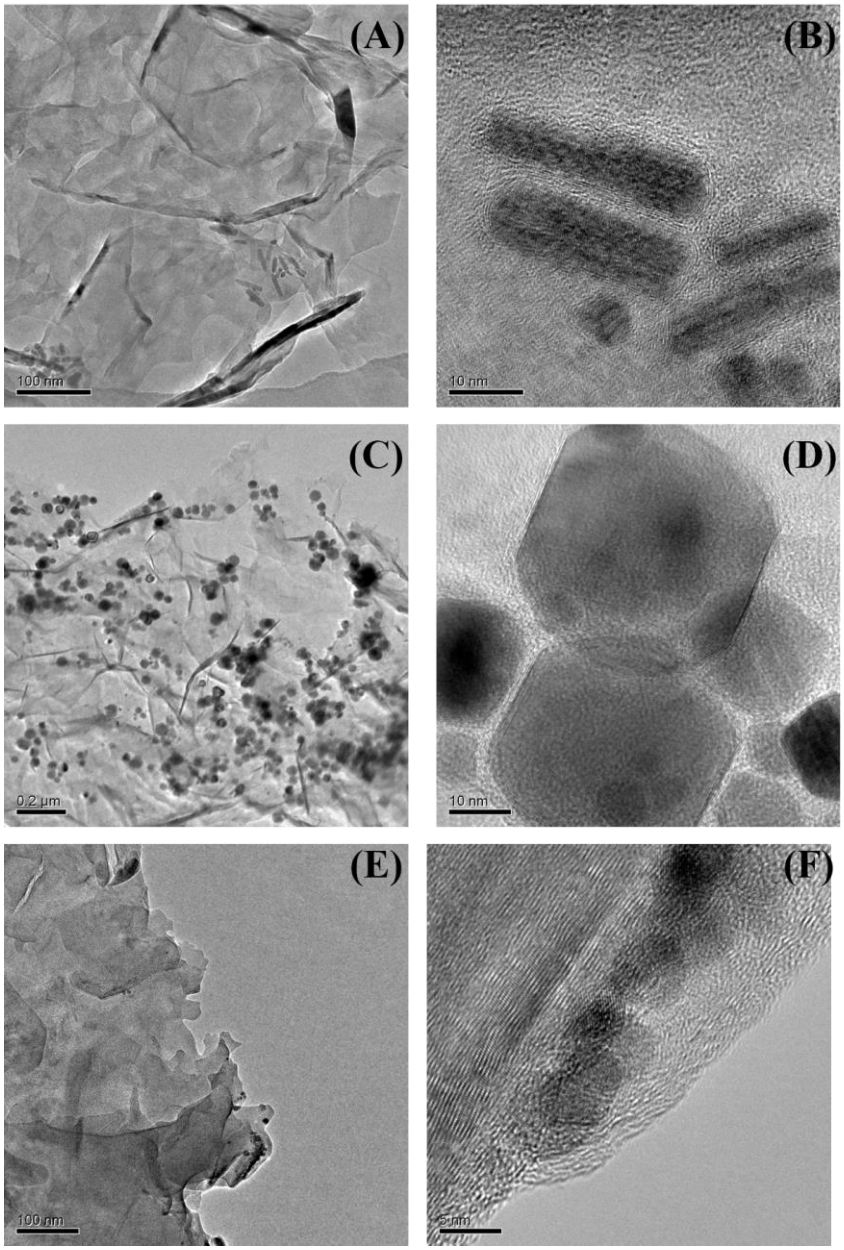

Figure S23: The HRTEM images of carbon nanostructures grown on metal-coated silicon substrates. (A) & (B) low and high resolution images of carbon nanostructures grown on Chromium coated silicon substrates. (C) & (D) low and high resolution images of carbon nanostructures grown on Copper coated silicon substrates. (E) & (F) low and high resolution images of carbon nanostructures grown on Nickel coated silicon substrate. Metal NPs act as the nucleation site for the CNWs nanostructure, but not all NPs act as the nucleation center, some of the NPs were inactivated and found to be lying on the CNWs.

27. SEM images of nanostructures at Cu thin-film/Si substrate.

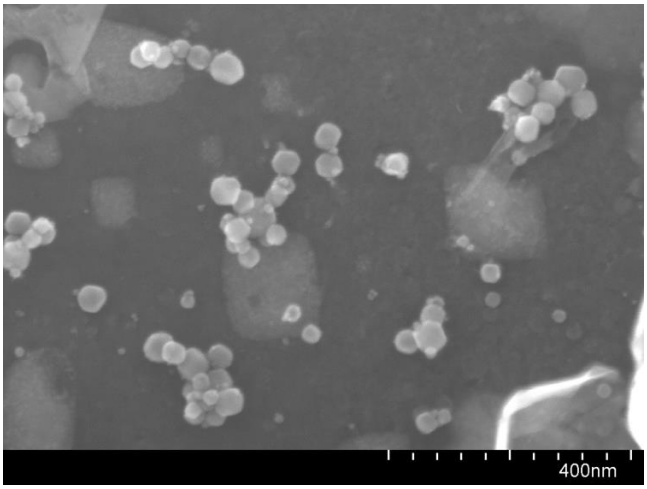

Figure S24: The SEM image of carbon nanostructures grown on cu-coated silicon substrates. A bunch of Cu NPs was lifted upwards by growing CNWs, and it is concluded that the CNWs grew in the vertical direction from the deposited amorphous layer.

28. Formation of a thick buffer layer.

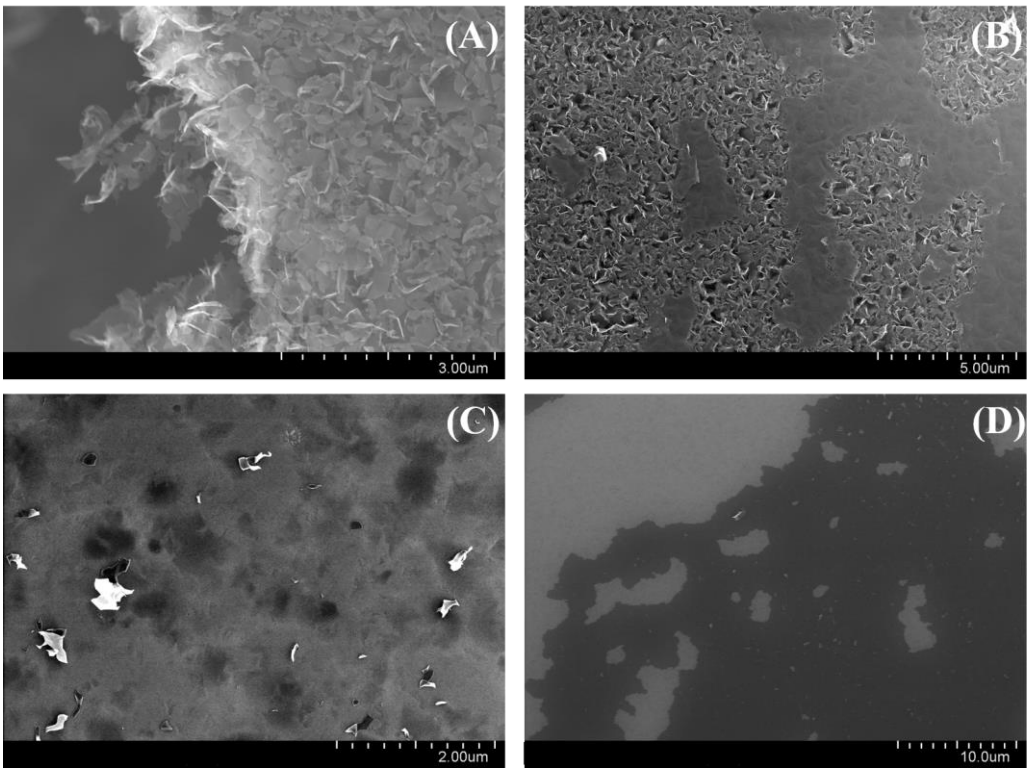

Figure S25: The SEM image of carbon nanostructures grown on silicon substrates. (A) FLGs nanostructures grew at lower methane gas flow rate (upside-down view). (B) CNWs nanostructures grew at higher methane gas flow rate, thick amorphous carbon layer can be seen sticking with CNWs (upside-down view). (C) Thin amorphous carbon layer was found (after peeling of the FLGs nanostructures). (D) Thick amorphous carbon carpet was found (after peeling of the CNWs nanostructures).

29. Anisotropic growth of FLGs nanostructures.

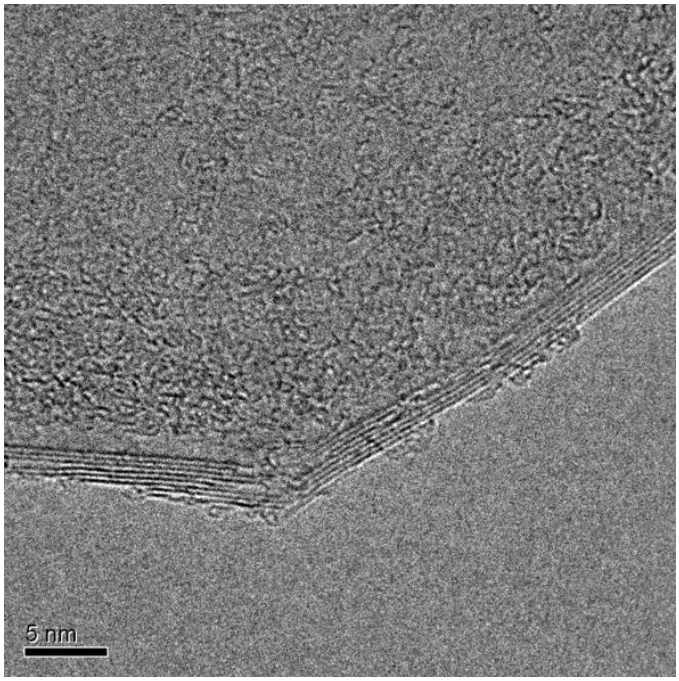

Figure S26: HRTEM images of FLGs nanostructures. FLGs growth was arrested by the growth anisotropy in a different direction, it might be because of defects heptagons and pentagons defects caused during growth, and these defects will disturb the diffusion of free carbon adatoms on the edges and FLGs growth comes to halt.

30. Effect of higher methane gas flow rate on nucleation sites.

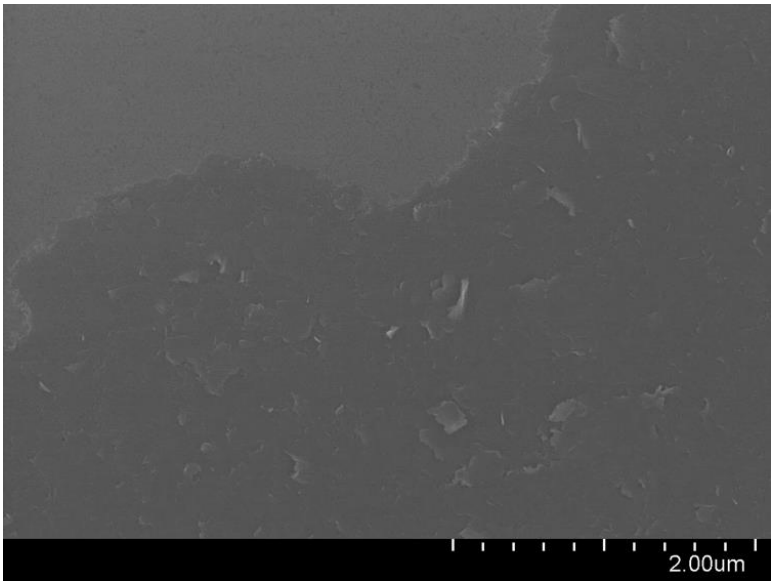

Figure S27: SEM images of CNWs after removal from the base substrate. CNWs were grown at high methane flow rate, as can be seen there is a thick amorphous layer attached to the base substrate. It will result in a high density of the nucleation sites with a large amount of amorphous carbon.

31. SEM images of 3D-HPG coated on CP and CC substrates via PECVD.

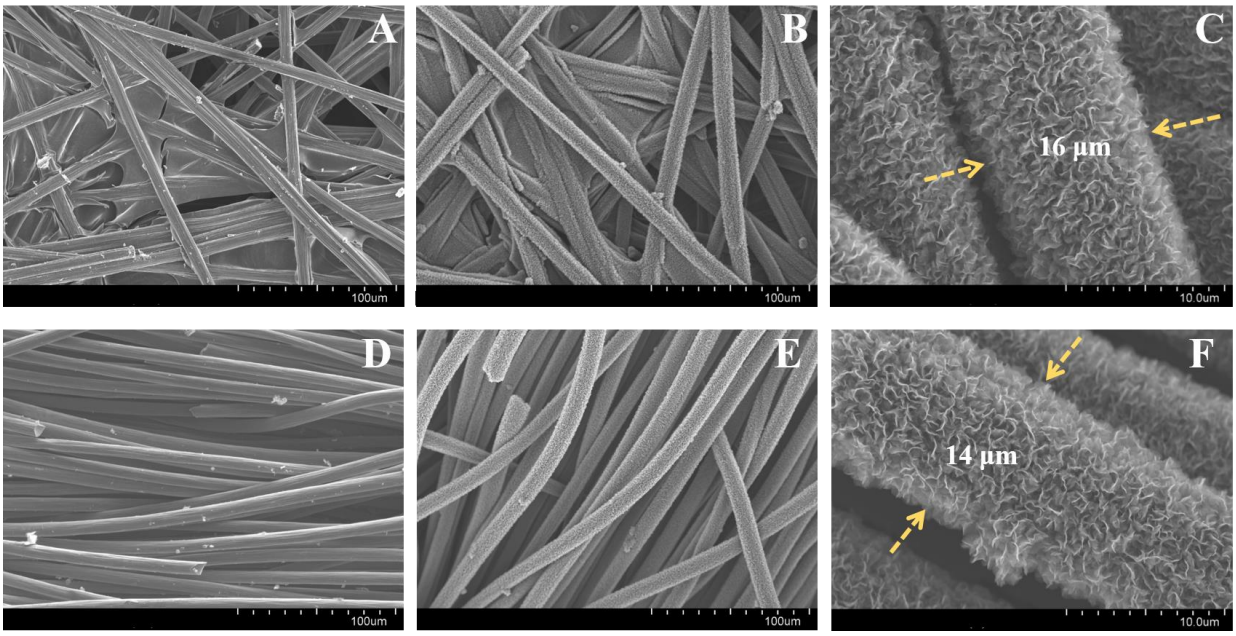

Figure S28: Three-dimensional (3D) interconnected hierarchically porous graphene (3D-HPG) was coated on CP and CC using PECVD. Figure (A), (B) and (C) shows the CP, low resolution 3D-HPG/CP and high resolution 3D-HPG/CP SEM images. Figure (C), (D) and (E) shows the CC, low resolution 3D-HPG/CC and high resolution 3D-HPG/CC SEM images. The average diameter of CP and CC fibers was 8.0 and 6.0 µm. After the nano-carbon coating, the average diameter was increased to 14.0 and 16.0 µm, respectively.

32. HRTEM images of typical 3D-HPG nanostructure grown at CC substrate.

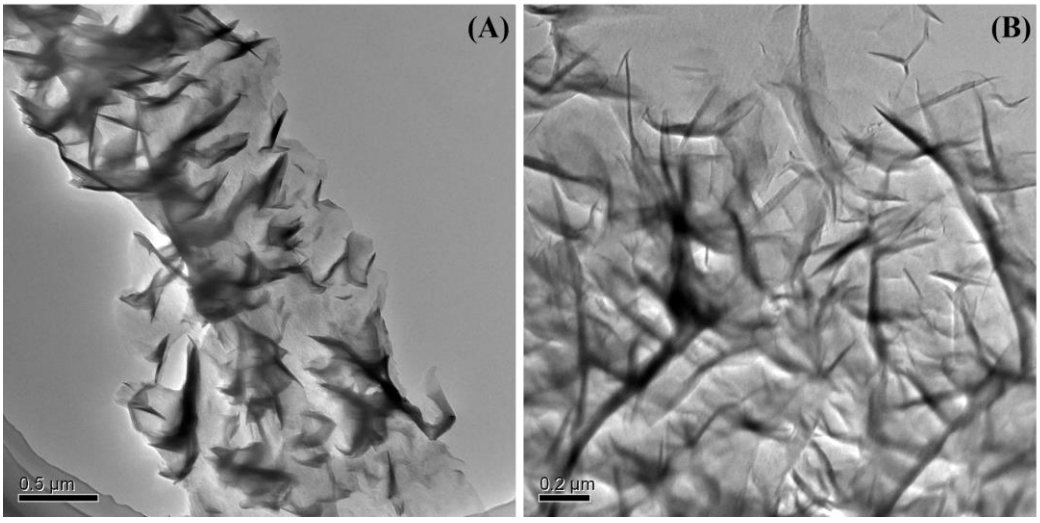

Figure S29: TEM images carbon nanostructure grown on CC. The nano-carbon coating comprises multiple graphene sheets with secondary fins and is composed of microporous structures.

33. The pore size distribution of 3D-HPG nanostructure.

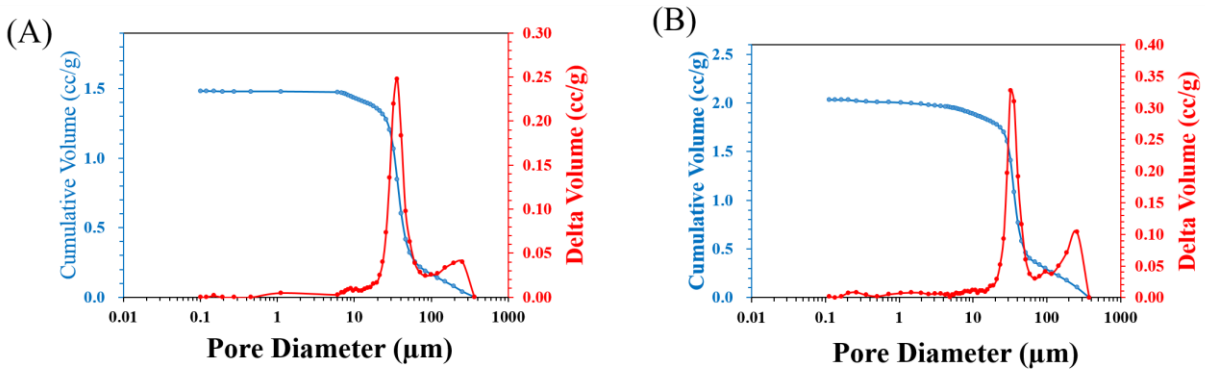

Figure S30: (A) The pore size distribution of CC substrate. (B) The pore size distribution of 3D-HPG/CC substrate, an additional peak with a pour diameter of ~300 nm was observed only for coated substrates. Nano-carbon coated CP and CC substrate' surface area was increased up to 3.7 times (up from 3.0 to 11.0 m^2/g) and 2.4 times (up from 18.7 to 48.9 m^2/g), respectively.

34. Table T3: Surface area and total pore volume 3D-HPGs nanostructures.

Sample Name	BET Surface Area (m^2/g)	BET Pore Volume (cm^3/g)
Carbon Paper	3	0.005
CNWs/Carbon Paper	11	0.034
Carbon Cloth	18.7	0.32
CNWs/Carbon Cloth	48.9	0.39

35. XPS wide and a detailed scan of C 1s of 3D-HPG nanostructures on CP substrate.

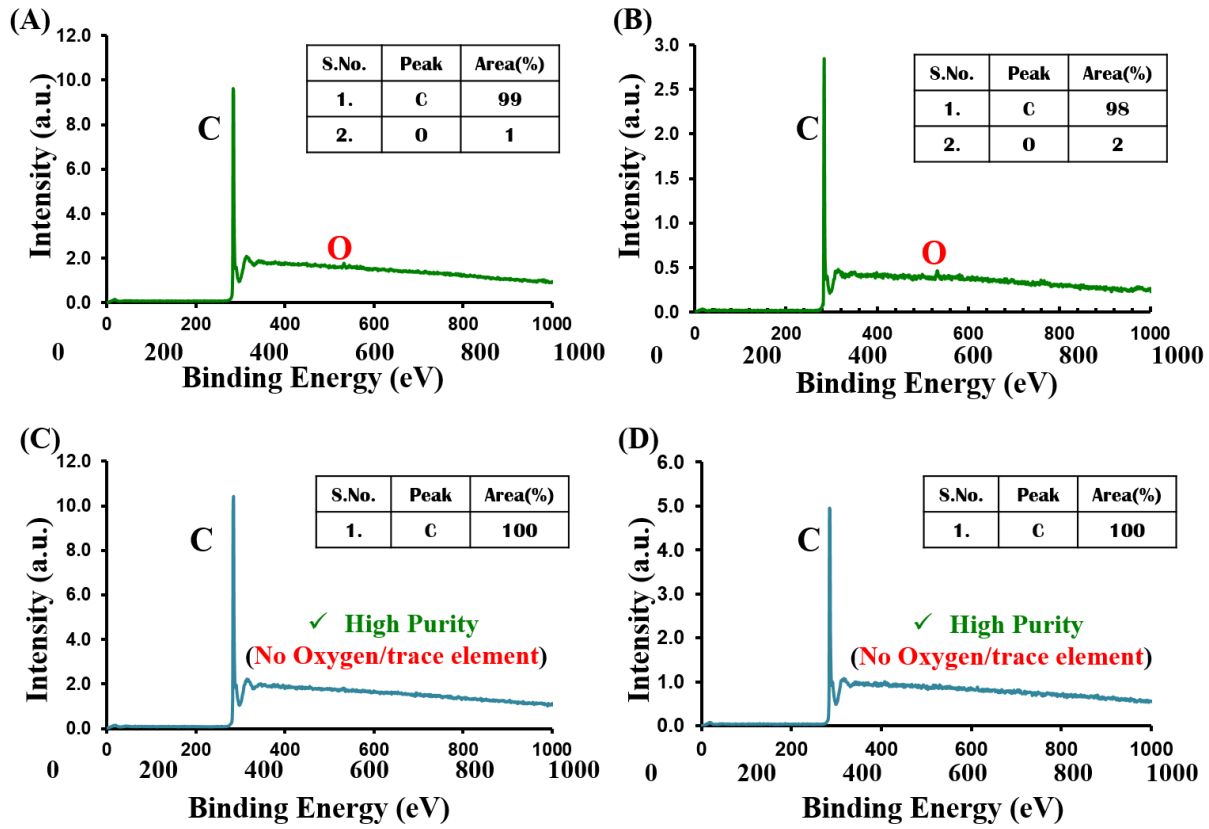

Figure S31: XPS wide scan. (A) Carbon Paper (alone). (B) Carbon Cloth (alone). (C) 3D-HPG coated on CP. (D) 3D-HPG coated on CC. There were evidence of oxygen prior to the 3D-HPG coating, however, after the coating the deposited nanostructure had no oxygen peak, indicating the high quality CNWs nanostructure.

36. XPS wide and a detailed scan of C 1s of 3D-HPGs nanostructures on CC substrate.

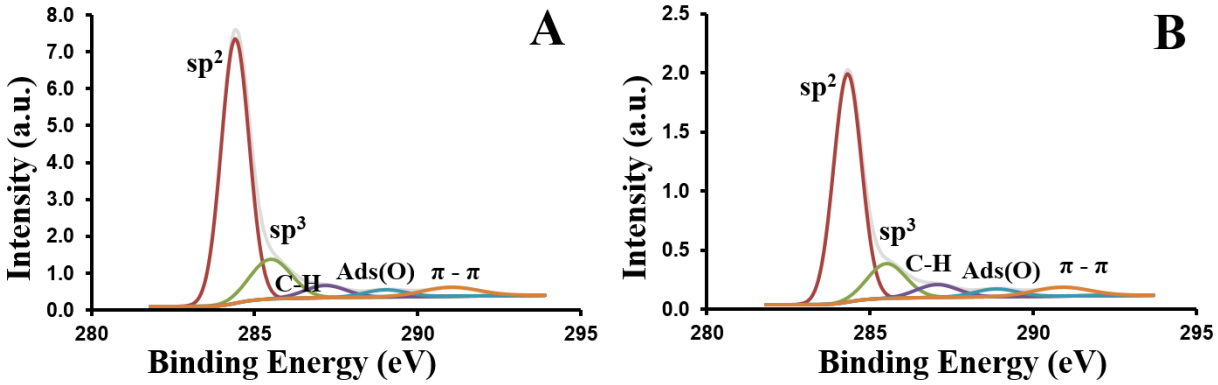

Figure S32: XPS scan of C 1s scan. (A) 3D-HPG/CP, five major peaks were found. Their contribution was found to be 68, 18, 5, 3, and 6%, respectively. (B) For 3D-HPG/CC specimen as well, five major peaks were found. Their contribution was found to be 67, 18, 5, 3, and 7%, respectively. 3D-HPG coated substrates were composed of pure elemental carbon.

37. Estimation of Electrochemical Surface Area (ECSA) for CP, 3D-HPG coated CP, CC, and 3D-HPG coated CC.

ECSA is calculated using three electrode setup consisting of nanostructure as the working electrode, Ag/AgCl as the reference electrode, and platinum wire as the counter electrode. 0.1M KOH is used as an electrolyte solution. The cyclic voltammetry (CV) graph of, each nanostructure, CP, CNW/CP, CC, and CNW/CC were recorded, respectively. From the CV graph, the voltage range of the non-Faradic region was taken into account. Subsequently, we recorded the CV at different scan rates (from 10 mV/sec to 100 mV/sec) in the non-Faradic region from voltage 1.16 V – 1.26 V. Then, using graph, current (mA) vs scan rate (mV/sec), the slope gives us the value of double layer capacitance (C_{dl}), which is used to calculate ECSA. The double layer capacitance (C_{dl}) was determined from the slope of the graph between current (mV) against scan rate in mVs^{-1} . The non-Faradic current density based electrochemically active surface area (ECSA) was estimated according to the equation: ECSA = C_{dl}/Cs , where C_s is the specific capacitance of the electrode and was taken as 0.040 $mFcm^{-2}$ in 0.1 M KOH electrolyte. Estimated ECSA are tabulated in Table 1. Please note that the sample CP was resistive in nature, therefore double-layer capacitance from that graph was not estimated.

Table: ECSA of CP, 3D-HPG coated CP, CC, and 3D-HPG coated CC specimen.

Sample Name	Area of Electrode	Electrochemical Surface Area (ECSA)
CP	6.1 cm^2	Not active
3D-HPG coated CP	5.36 cm^2	0.066 cm^2
CC	6.1 cm^2	0.111 cm^2
3D-HPG coated CC	7.8 cm^2	0.185 cm^2

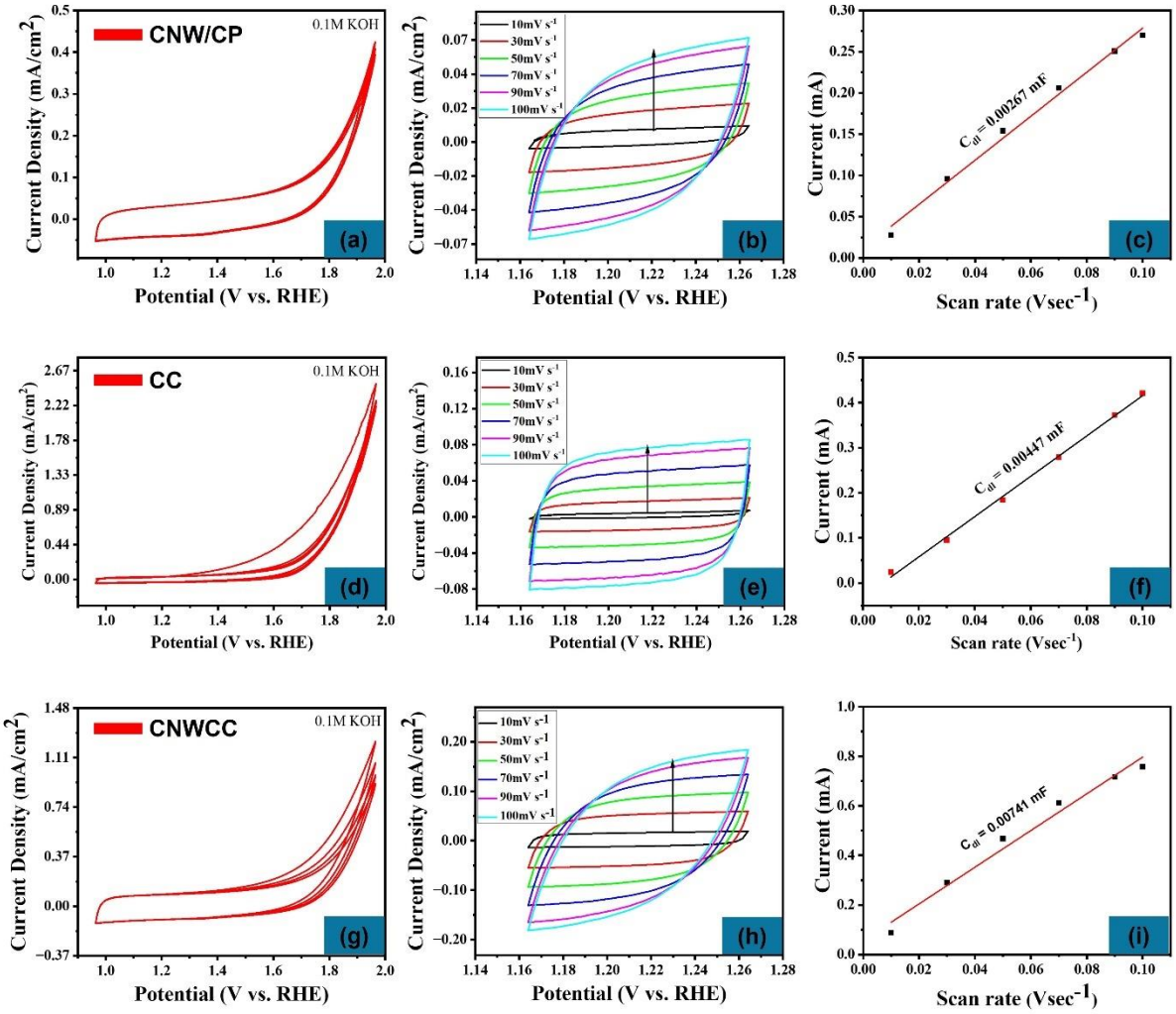

Figure 33S: Results of electrochemical studies performed to calculate ECSA. (a), (d) and (g) are Cyclic voltammetry of CP, 3D-HPG coated CP, CC, and 3D-HPG coated CC. (b), (e) and (h) CV curve at different scan rate from 10 $mVsec^{-1}$ to 100 $mVsec^{-1}$ for CP, 3D-HPG coated CP, CC, and 3D-HPG coated CC. (c), (f) and (i) graph represents current against the scan rate showing the double-layer capacitance (C_{dl}) extracted from the corresponding CVs for CP, 3D-HPG coated CP, CC, and 3D-HPG coated CC.

38. Charge and Discharge profile of 3D-HPG coated CP and CC electrodes at 0.1 mA and 0.3 mA.

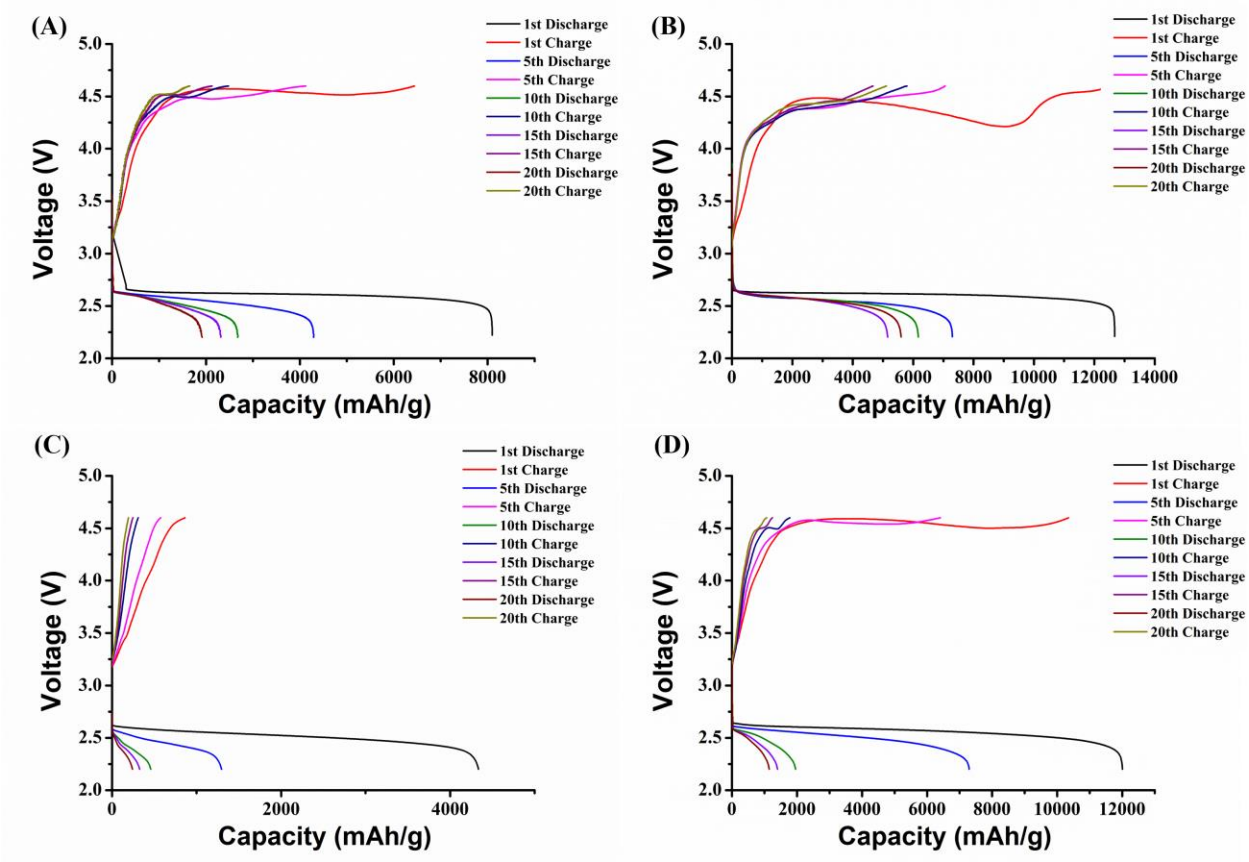

Figure S34: The cyclic performance of Li-oxygen battery. (A) & (C) The cyclic performance of 3D-HPG coated CP at 0.1 mA and 0.3 mA. (B) & (D) The cyclic performance of 3D-HPG coated CC at 0.1 and 0.3 mA, respectively. The charge curve showed the voltage plateau at 4.5 V, and it was relatively high. It could be caused by the deposition of Li_2CO_3 during discharge, as confirmed by Raman. It is known that Li_2O_2 is decomposed around 4.5 V. Although Li_2CO_3 was hardly decomposed during charge in a non-aqueous electrolyte system, a high charge voltage is required to decompose the Li_2CO_3. The round trip efficiency (the ratio of discharge to charge voltage) in the present cell without any additional catalyst was 58%, which is in accordance with the pure carbon cathode. As the charge/discharge cycle progresses, discharge capacity decreased, and capacity retention was over ~25% even after 20 discharge/charge cycles.

39. SEM images of the CC and 3D-HPG coated CC at 0.3 mA.

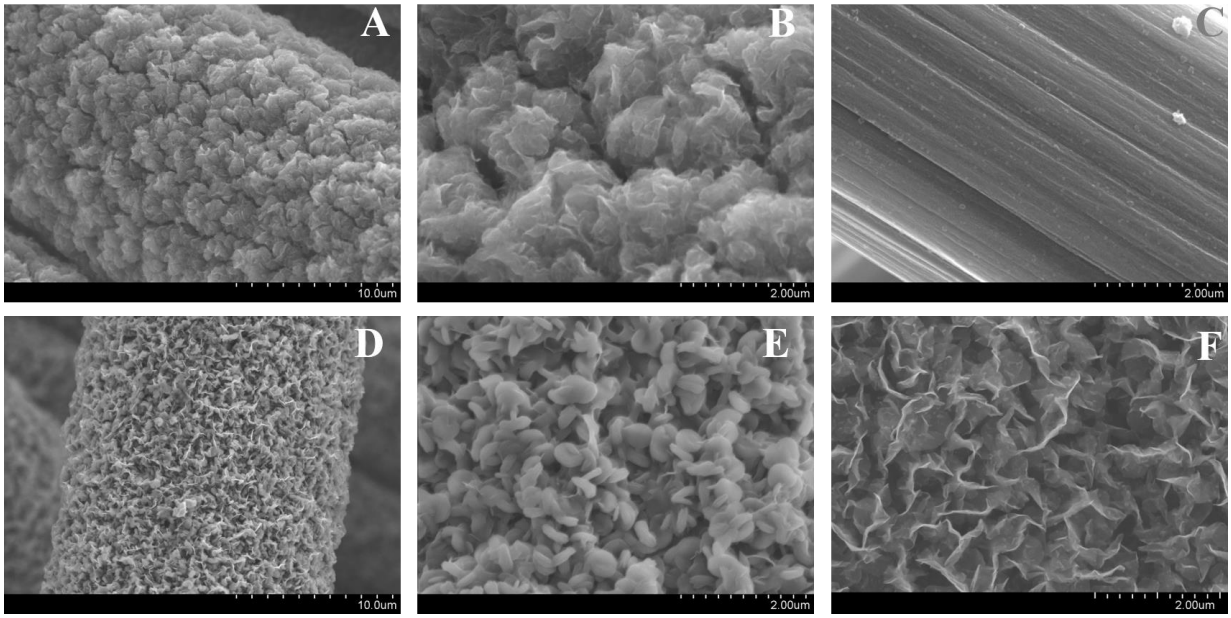

Figure S35: Low and high resolution SEM images in figure (A) and (B) shows that the discharge product@CC after initial cycle (discharge 0.3 mA), (C) shows the electrode after 20 discharge/charge cycles. Figures (D) and (E) show discharge product@3D-HPG after initial cycle (discharge 0.3), whereas figure (F) shows the electrode after 20 discharge/charge cycles. As can be seen that the show that the 3D-HPG electrodes discharge product could not decompose as the cycling progressed.

40. SEM images of the CC and 3D-HPG coated CC at 0.3 mA.

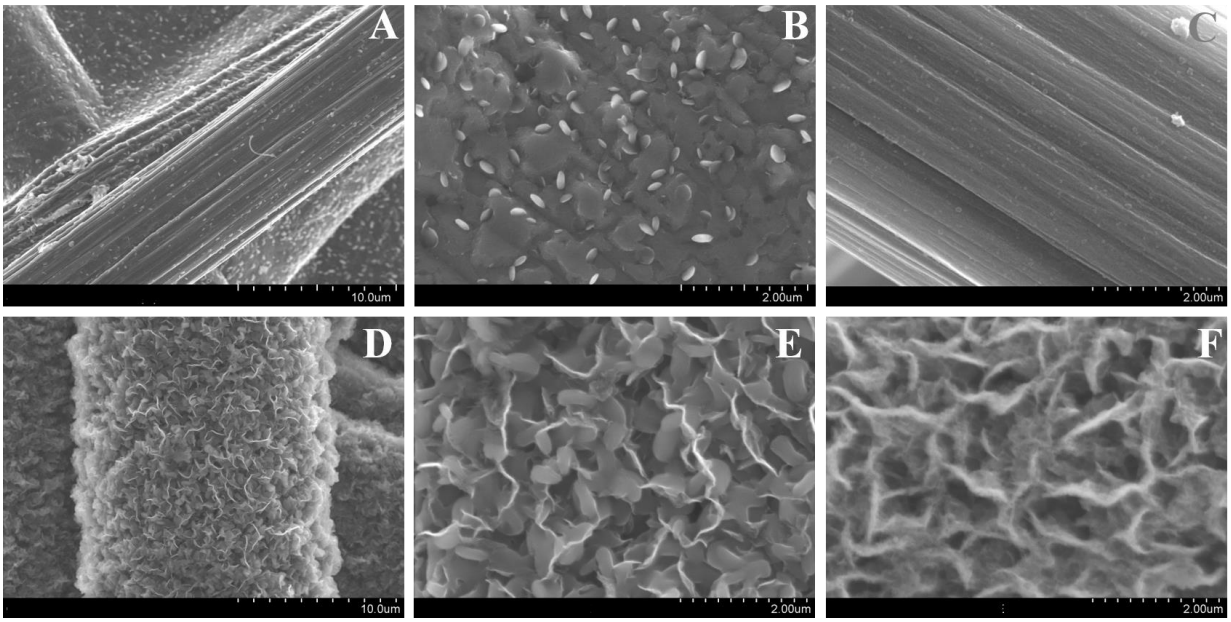

Figure S36: Low and high resolution SEM images in figure (A) and (B) shows that the discharge product@CP after initial cycle (discharge 0.3 mA), (C) shows the electrode after 20 discharge/charge cycles. Figures (D) and (E) show discharge product@3D-HPG after initial cycle (discharge 0.3), whereas figure (F) shows the electrode after 20 discharge/charge cycles. As can be seen that the show that the 3D-HPG electrodes discharge product could not decompose as the cycling progressed.

41. Point-localized EDS of 3D-HPG coated CP and CC electrodes.

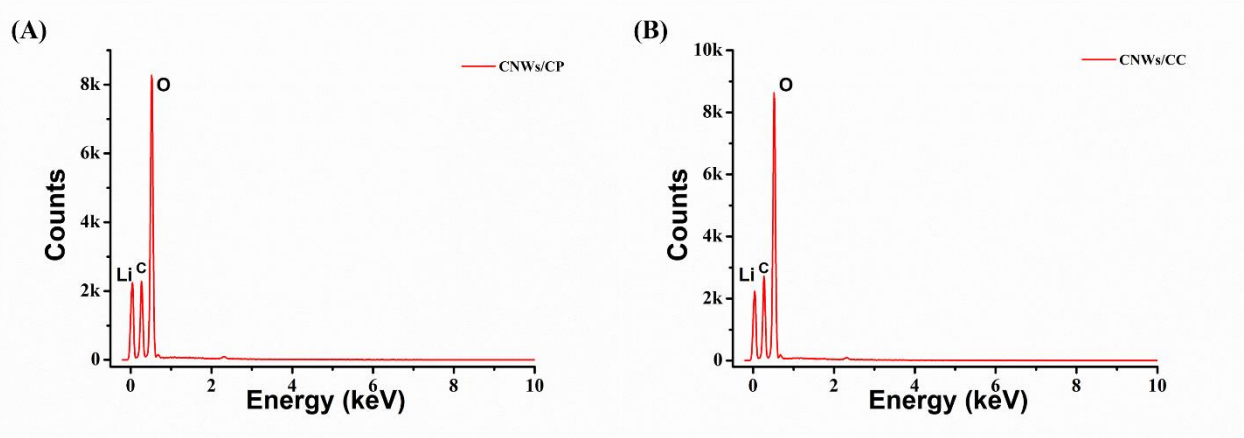

Figure S37: The point-localized EDS spectrums in figure S36 show that the discharge product of 3D-HPG coated CP and CC electrodes were composed of lithium and oxygen.

42. The charge and discharge product of 3D-HPG coated CC Raman spectra.

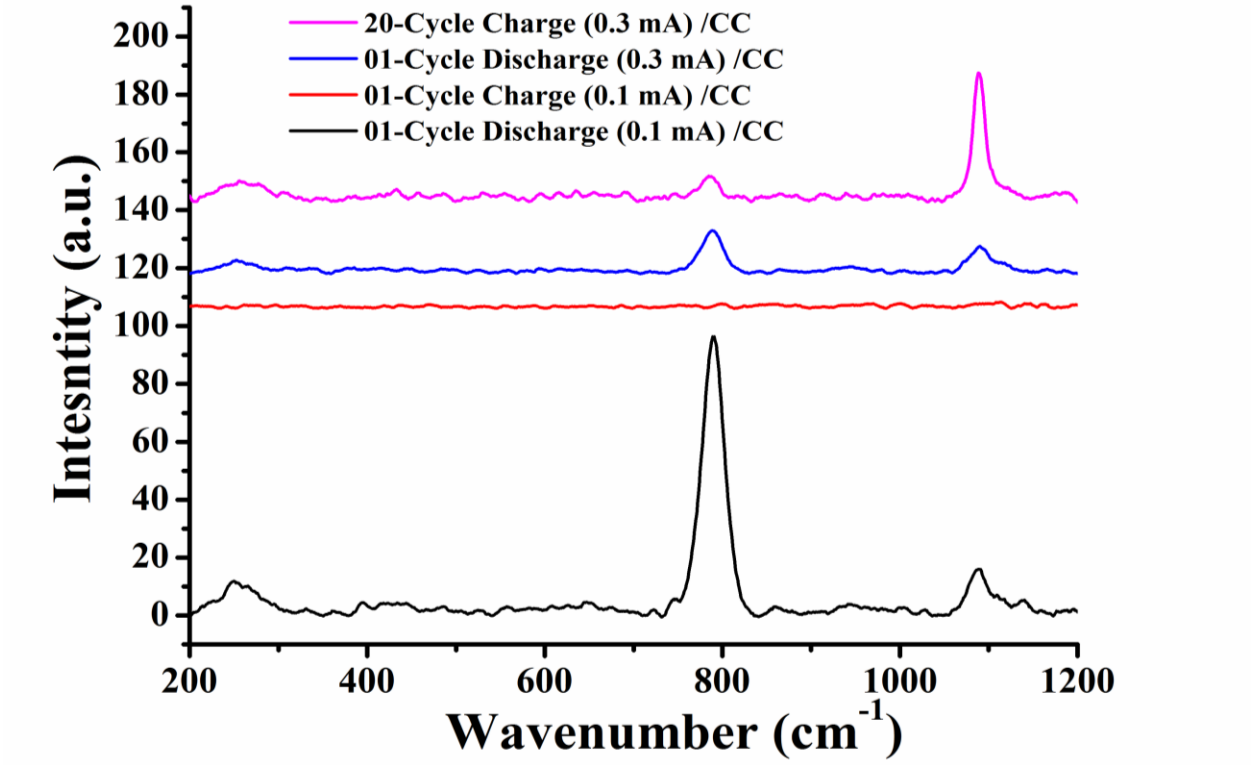

Figure S38: The charge and discharge product of 3D-HPG coated CC Raman spectra. At Initial discharge (01-cycle discharge) showed three peaks; 250 and 790cm^{-1} correspond to lithium peroxide (Li_2O_2), whereas peak at1090 cm^{-1} was attributed to lithium carbonate (Li_2CO_3). After the initial charge (1-cycle charge), the deposited product was wholly removed from the 3D-HPG coated CC electrode. However, with an increase in the discharge current, the ratio between Li_2CO_3 and Li_2O_2 was increased. Furthermore, this ratio continues to increase after cycling (20 cycle charge @ 0.3 mA).

43. The charge and discharge product of 3D-HPG coated CP Raman spectra.

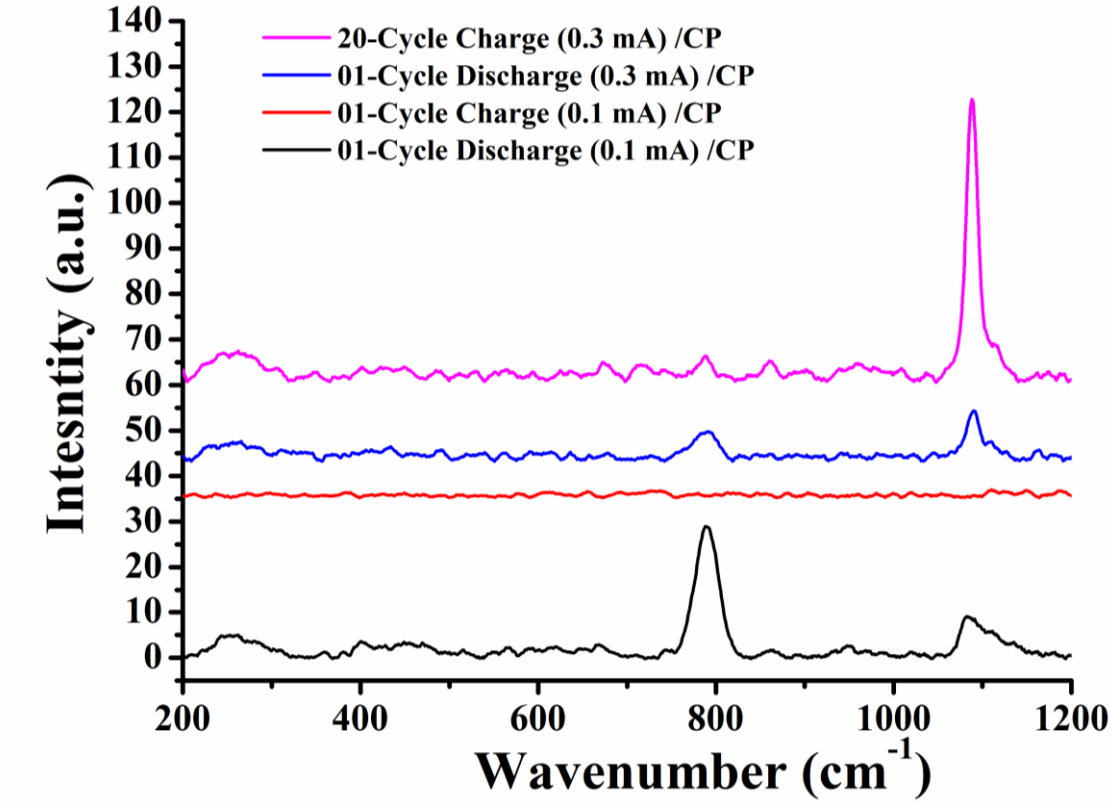

Figure S39: The charge and discharge product of 3D-HPG coated CP Raman spectra. At Initial discharge (01-cycle discharge) showed three peaks; 250 and 790cm^{-1} correspond to lithium peroxide (Li_2O_2), whereas peak at1090 cm^{-1} was attributed to lithium carbonate (Li_2CO_3). After the initial charge (1-cycle charge), the deposited product was wholly removed from the 3D-HPG coated CC electrode. However, with an increase in the discharge current, the ratio between Li_2CO_3 and Li_2O_2 was increased.